Global ray tracing simulations of the SABER gravity wave climatology

Peter Preusse,[1] Stephen D. Eckermann,[2] Manfred Ern,[1] Jens Oberheide,[3]
Richard H. Picard,[4] Raymond G. Roble,[5] Martin Riese,[1] James M. Russell III,[6]
and Martin G. Mlynczak[7]

[1] Since February 2002, the SABER (sounding of the atmosphere using broadband emission radiometry) satellite instrument has measured temperatures throughout the entire middle atmosphere. Employing the same techniques as previously used for CRISTA (cryogenic infrared spectrometers and telescopes for the atmosphere), we deduce from SABER V1.06 data 5 years of gravity wave (GW) temperature variances from altitudes of 20 to 100 km. A typical annual cycle is presented by calculating averages for the individual calendar months. Findings are consistent with previous results from various satellite missions. Based on zonal mean, SABER data for July and zonal mean GW momentum flux from CRISTA, a homogeneous and isotropic launch distribution for the GROGRAT (gravity wave regional or global ray tracer) is tuned. The launch distribution contains different phase speed mesoscale waves, some of very high-phase speed and extremely low amplitudes, as well as waves with horizontal wavelengths of several thousand kilometers. Global maps for different seasons and altitudes, as well as time series of zonal mean GW squared amplitudes based on this launch distribution, match the observations well. Based on this realistic observation-tuned model run, we calculate quantities that cannot be measured directly and are speculated to be major sources of uncertainty in current GW parameterization schemes. Two examples presented in this paper are the average cross-latitude propagation of GWs and the relative acceleration contributions provided by saturation and dissipation, on the one hand, and the horizontal refraction of GWs by horizontal gradients of the mean flow, on the other hand.

1. Introduction

[2] Gravity waves (GWs) are an important dynamical driving force for the middle atmosphere. They are believed to be the main drivers of the mesospheric circulation and the cold summer mesopause [e.g., *McLandress*, 1998], to provide about half of the momentum required for driving the quasibiennial oscillation (QBO) in the tropics [*Dunkerton*, 1997], and to contribute significantly to the Brewer-Dobson circulation [*Alexander and Rosenlof*, 2003]. However, GW parameterizations used in global modeling are highly simplified. In these schemes GWs are assumed to propagate purely vertically and remain inside the same general circulation model (GCM) grid column, not to change their horizontal propagation direction and to transfer momentum to the large-scale flow merely by wave-breaking processes [*Hines*, 1997; *Warner and McIntyre*, 1999; *Alexander and Dunkerton*, 1999; *Medvedev and Klaassen*, 2000].

[3] In addition, the launch distributions of these nonorographic GW parameterization schemes are very simplified. In order to investigate the validity of these assumptions and simplifications, we need global observations, a model which avoids these simplifications, and a launch distribution that allows the model to reproduce the observations.

[4] In this paper we have three main aims:

[5] 1. Deduce a global climatology of GWs from SABER temperatures.

[6] 2. Infer a GW launch distribution complying with these measurements.

[7] 3. Test assumptions made in GW parameterization schemes.

[1]Institute of Chemistry and Dynamics of the Geosphere, ICG-1: Stratosphere, Research Center Juelich, Juelich, Germany.
[2]Space Science Division, Naval Research Laboratory, Washington, DC, USA.
[3]Department of Physics, Wuppertal University (BUGW), Wuppertal, Germany.
[4]Air Force Research Laboratory, Hanscom Air Force Base, Massachusetts, USA.
[5]High Altitude Observatory, National Center for Atmospheric Research, Boulder, Colorado, USA.
[6]Department of Physics, Hampton University, Hampton, Virginia, USA.
[7]NASA Langley Research Center, Hampton, Virginia, USA.

Report Documentation Page			*Form Approved* *OMB No. 0704-0188*

1. REPORT DATE **06 FEB 2009**	2. REPORT TYPE		3. DATES COVERED **00-00-2009 to 00-00-2009**
4. TITLE AND SUBTITLE **Global ray tracing simulations of the SABER gravity wave climatology**			5a. CONTRACT NUMBER
			5b. GRANT NUMBER
			5c. PROGRAM ELEMENT NUMBER
6. AUTHOR(S)			5d. PROJECT NUMBER
			5e. TASK NUMBER
			5f. WORK UNIT NUMBER
7. PERFORMING ORGANIZATION NAME(S) AND ADDRESS(ES) **Naval Research Laboratory,Space Science Division,Washington,DC,20375**			8. PERFORMING ORGANIZATION REPORT NUMBER
9. SPONSORING/MONITORING AGENCY NAME(S) AND ADDRESS(ES)			10. SPONSOR/MONITOR'S ACRONYM(S)
			11. SPONSOR/MONITOR'S REPORT NUMBER(S)
12. DISTRIBUTION/AVAILABILITY STATEMENT **Approved for public release; distribution unlimited**			
13. SUPPLEMENTARY NOTES			
14. ABSTRACT			
15. SUBJECT TERMS			

16. SECURITY CLASSIFICATION OF:			17. LIMITATION OF ABSTRACT	18. NUMBER OF PAGES	19a. NAME OF RESPONSIBLE PERSON
a. REPORT **unclassified**	b. ABSTRACT **unclassified**	c. THIS PAGE **unclassified**	**Same as Report (SAR)**	**25**	

Standard Form 298 (Rev. 8-98)
Prescribed by ANSI Std Z39-18

[8] There has been previous work on all three topics in the literature and an overview is given in Appendix A. The current study advances from previous work in several ways.

[9] Infrared limb sounding covers a wide range of horizontal and vertical wavelengths which is not assessed by any other satellite instrument [*Preusse et al.*, 2008]. However, previous studies on GWs inferred from infrared limb sounding focused on episodes only. In this study we infer a GW climatology for a typical annual cycle from 4 years of temperature measurements by the Sounding of the Atmosphere using Broadband Emission Radiometry (SABER) infrared limb sounder (see section 2). Apart from the wavelength range this climatology is unique in covering the whole middle atmosphere from 20 to 100 km altitude.

[10] Recently, two studies have inferred tunable parameters of semiempirical GW launch spectra [*Alexander and Rosenlof*, 2003; *Ern et al.*, 2006]. The large altitude coverage by the SABER climatology now makes a different approach feasible. Features unique to different parts of the GW spectrum allow for a forward construction of a plausible wave spectrum. This approach is more complex and increases the number of free parameters. In addition, we restrict ourselves to zonal mean boreal summer data from SABER and zonal mean estimates of absolute values of momentum flux from CRISTA for the tuning of the launch distribution. Global maps and the annual cycle then provide independent tests for the chosen approach. We can determine limitations of such a simplified, homogeneous, isotropic and temporal constant launch distribution.

[11] Several assumptions made in the classical GW parameterization schemes recently have been challenged. Oblique wave propagation was included in a ray-tracing parameterization of GWs forced by deep convection [*Song and Chun*, 2008]. In addition to wave dissipation, momentum transfer associated with horizontal refraction was postulated on theoretical grounds to force the large-scale winds [*Bühler and McIntyre*, 2003]. *Hasha et al.* [2008] have studied the impact of this effect on orographic GW drag parameterization. Gravity wave induced mean wind-forcing calculated in this paper will provide a first realistic estimate of the overall impact of these effects.

[12] In our paper we will base on one main assumption: The approach of an isotropic launch distribution, which is spatially homogeneous or has a simple latitude dependence, is used in classical nonorographic GW parameterization schemes. We follow this approach in this paper for two reasons. First, we infer the spectral launch distribution from the global GW distribution in terms of altitude-height cross sections. This is only possible if we assume the spatial launch distribution. Second, in this way we can test the limits of this widely used approach. The approach is tested (and supported) using a much larger data set than used for the tuning of the launch distribution. Nevertheless, the deduced launch distribution is valid only in the frame of this assumption.

[13] The technique for extracting GW signals from SABER temperature profiles is described in section 2. Section 3 introduces the Gravity wave Regional Or Global RAy Tracer (GROGRAT) and the background atmosphere used for the ray tracing experiments. The "optimal" launch distribution of GWs is inferred in section 4. In section 5, global maps as well as zonal mean cross sections of a typical annual cycle composed from almost 5 years of SABER data are compared

to GROGRAT modeling results based on this launch distribution. In section 6 the GROGRAT model results are used to estimate average cross-latitude propagation and GW-induced mean flow accelerations. A summary and discussion are given in section 7.

2. Instrument and Analysis Technique

[14] The SABER instrument [*Mlynczak*, 1997; *Russell et al.*, 1999; *Yee et al.*, 2003] is an infrared emission limb sounder covering the upper troposphere, stratosphere, mesosphere and lower thermosphere. SABER is on board of the Thermosphere Ionosphere Mesosphere Energetics and Dynamics (TIMED) satellite on a $74°$ inclination orbit. In this paper we use temperatures from version 1.06 (V1.06) retrievals. Temperatures are retrieved from the main CO_2 ν_2 emission at 15 μm. A coupled retrieval algorithm evaluates CO_2 densities and temperatures simultaneously from 4.3 μm and 15 μm emissions and takes into account nonlocal thermodynamic equilibrium (NLTE) effects [*Mertens et al.*, 2001, 2004]. NLTE effects and interaction with chemistry start to exert an influence above ∼70 km altitude and become increasingly important in the mesopause and lower thermosphere region [*Kutepov et al.*, 2006]. Accordingly, SABER temperature errors are 1–2 K for altitudes below 80 km, and increase above this altitude [*Mertens et al.*, 2001; *Remsberg et al.*, 2008]. The most recent estimate *Remsberg et al.* [2008] for V1.07 states a preliminary absolute temperature error of 3 K and a noise error of 1.2 K at 85 km altitude. In addition, a second particularly difficult region to retrieve is the tropical tropopause, because measurements below it are likely to be cloud contaminated and because of the very sharp knee in tropopause temperatures.

[15] The TIMED satellite performs six yaw maneuvers per year, changing from a south-looking ($83°S–52°N$) to a north-looking ($52°S–83°N$) geometry and vice versa. The relative times of the yaw maneuvers during the year are the same for different years, so that, for instance, SABER always views to the south in August.

[16] SABER temperatures between 20 and 100 km altitude are analyzed employing the algorithms described by *Preusse et al.* [2002]. The global background atmosphere is estimated by a zonal wave number 0–6 Kalman filter and subtracted from the individual profiles. This approach captures long period planetary waves and, by detrending ascending and descending orbit legs separately, also tidal signatures [*Preusse et al.*, 2001a]. In contrast to the vertical detrending approach used for radiosonde and GPS climatologies [e.g., *Tsuda et al.*, 2000], this horizontal scale separation approach preserves the vertical spectral information on GWs in the data. Horizontal wavelengths range between the visibility limit of 100–200 km [*Preusse et al.*, 2002] and zonal wave number 7. The upper wavelength limit, however, is probably not a serious constraint, since horizontal wavelength estimates from CRISTA [*Preusse et al.*, 2006] indicate that the upper end of the horizontal wavelength distributions is limited by physical processes rather than by the analysis method.

[17] After separation from the background atmosphere, the residual temperature profiles are analyzed by a combination of maximum entropy method (MEM) and harmonic analysis, thus providing the amplitudes, vertical wave-

lengths and phases of the two strongest wave components at each altitude of a measured profile [*Preusse et al.*, 2002]. The width of the sliding vertical window of the harmonic analysis is 10 km.

[18] In this paper, we focus on seasonal variations which are persistent for different years. We therefore bin the data according to calendar months for the almost 5-year time series from February 2002 to December 2006, so that, for instance, July values contain data from July 2002, 2003, 2004, 2005 and 2006.

3. Global Gravity Wave Model

3.1. Description of Ray Tracer

[19] The observed GW distributions are compared to results from global GW ray tracing experiments using the Gravity wave Regional Or Global RAy Tracer (GROG-RAT). A full description of the GROGRAT model can be found in the works of *Marks and Eckermann* [1995] and *Eckermann and Marks* [1997] and we here give a brief summary only. GROGRAT is based on the nonhydrostatic, rotational GW dispersion relation

$$\hat{\omega}^2 = \frac{N^2(k^2 + l^2) + f^2\left(m^2 + \frac{1}{4H^2}\right)}{k^2 + l^2 + m^2 + \frac{1}{4H^2}}, \qquad (1)$$

where $\hat{\omega}$ is the intrinsic frequency, N is the buoyancy frequency, k, l and m are the wave numbers in x, y and z directions in a local geophysical coordinate system with x pointing to the east, respectively, and H is the density scale height.

[20] The ray tracing equations take into account refraction of the wave vector due to vertical as well as horizontal gradients of the background atmosphere and meridional gradients of the Coriolis force. In the absence of dissipative processes wave action density is conserved along the ray traces and amplitudes are calculated accordingly. Amplitudes are limited by saturation due to vertical dynamic instability following the works of *Fritts and Rastogi* [1985] and *Marks and Eckermann* [1995]. In addition, dissipative processes such as radiative and turbulent damping, which affect waves with amplitudes well below any saturation threshold for wave breaking, are parameterized.

3.2. Setup of Model Experiment

[21] The representativeness of a ray tracing experiment largely depends on the choice of the background atmosphere. In the present study, we use European Centre for Medium-Range Weather Forecasts (ECMWF) reanalyses from 0 to 50 km altitude and winds and temperatures from the Thermosphere Ionosphere Mesosphere Energetics General Circulation Model (TIME-GCM) [*Roble and Ridley*, 1994] from 40 to 100 km altitude, with the two smoothly blended in the overlap region from 40 to 50 km altitude following the work of *Preusse et al.* [2008]. ECMWF reanalysis data are used in numerous scientific studies and capture the synoptic scale features of the troposphere and stratosphere well [*Borsche et al.*, 2007; *Ern et al.*, 2008]. For the mesosphere and above so far assimilated data are, in general, not available. In order to approximate the actual atmospheric state in the upper stratosphere and MLT the

known state in the stratosphere is projected upward by means of a GCM. We use data from a TIME-GCM experiment conducted especially for the TIMED mission. The TIME-GCM is nudged at 30 km altitude to NCEP reanalyses and radiation-forced migrating tidal components at the lower boundary are provided from the GSWM tidal model [*Hagan et al.*, 1995]. The GCM was run continuously from January 2002 to December 2004 and has been used, for example, to analyze tides [*Oberheide et al.*, 2006]. Combining ECMWF and TIME-GCM data, we therefore generate a background atmosphere representing, to the best of our knowledge, the actual conditions at the time of the SABER observations. However, it should be kept in mind that the GCM results for the MLT are only an upward projection of the stratospheric dynamics and have not the same reliability as the stratospheric data which are well constrained by assimilated data.

[22] For the ray-tracing model runs, the background atmosphere winds and temperatures are interpolated to a regular grid with a resolution of 2.5° latitude and 3.75° longitude on 41 pressure levels corresponding to an altitude spacing of 2.5 km. Latitudes range from 85 S to 85 N (GROGRAT does not propagate rays across the pole). Ray tracing calculations are performed for snap shots at respective fixed local times and dates. Where temporally averaged data are shown, the ray tracer is performed for the individual time steps and the results are averaged afterward.

[23] Criteria for terminating the ray calculations are discussed in some depth by *Preusse et al.* [2008]. In addition to processes related to critical level filtering rays are terminated when they reach the latitudinal or upper boundary. Wave reflection does not occur in our simulations since the long horizontal wavelengths considered prevent that the intrinsic frequency $\hat{\omega}$ approaches the buoyancy frequency N. The vertical interpolation and coarse vertical grid resolution (2.5 km) of the background atmosphere smoothen the tropical tropopause which reduces WKB violations. In general, we calculate rays past WKB limits.

[24] The initial launch conditions for the waves follow the same overall approach used by *Preusse et al.* [2006] in their GROGRAT-SABER comparison study. A wave is initialized at its launch latitude, longitude and altitude with a specific propagation direction, horizontal wavelength, phase speed and amplitude. In order to perform a systematic analysis we launched waves homogeneously and isotropically on a regular grid of 20° longitude × 5° latitude in eight equispaced azimuth directions, i.e., every 45° starting from due east. Such a "single spectral component experiment" (SCE) is defined by the GW horizontal wavelength λ_h, ground-based phase speed c_h, peak horizontal wind amplitude $\hat{u}_l$ at launch level and launch altitude. (Note that SABER measures temperatures, but launch amplitudes for GROGRAT are specified in terms of wind.) Combining several SCEs, we can emulate a full launch spectrum.

[25] The SCE launch grid is given in Figure 1. The launch locations are indicated by black asterisks. At each launch location rays are launched into eight azimuth directions. In addition, for waves launched at the zero meridian raypaths resulting for 15 July 2003 are shown. The color indicates altitude. Waves propagating against the wind attain large vertical group velocities and quickly reach the mesosphere, whereas waves propagating with the wind "drift" large
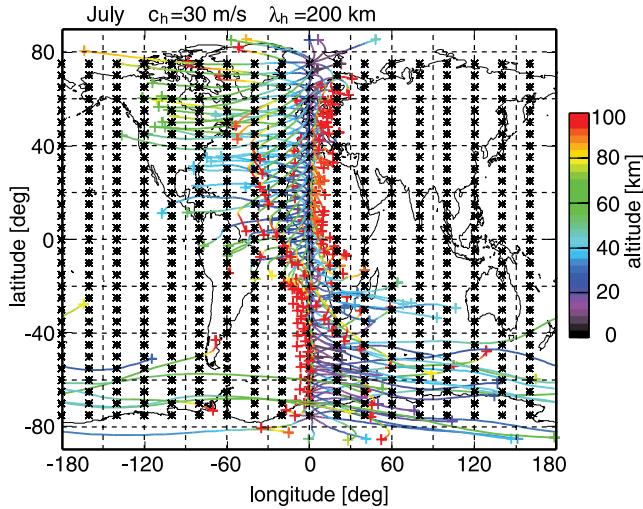
Figure 1. Launch distribution of one SCE (λ_h = 200 km, c = 30 m s^{-1}, $\hat{u}_l$ = 1 m s^{-1}). At each black asterisk, eight rays are launched in eight different directions. Rays starting from 0° longitude are shown as an example. Color code gives altitude along ray trajectories. The plus sign shows the location where the ray is terminated.

distances downstream in taking much longer to propagate vertically.

[26] Guided by previous global GW modeling studies as well as studies of GWs in a GCM [*Alexander*, 1998; *Manzini and McFarlane*, 1998; *Ern et al.*, 2004, 2006] we chose a launch altitude of 5 km for all SCEs. Due to computational costs, we were forced to restrict the number

of SCEs. An overview of all SCEs which we have considered is given in Table 1. We therefore launch only horizontal wavelengths which match the observational filter of SABER and in particular do not launch short horizontal wavelength waves. As discussed in some depth by *Preusse et al.* [2006], we know from previous studies that a combination of medium and long horizontal wavelength waves is required. The medium horizontal scale GWs are represented by two horizontal wavelengths (200 km and 500 km), which cover the full range of phase speeds. Longer horizontal wavelength GWs are represented by using only three different phase speeds, and in particular, only for c_h = 30 m s^{-1} do we use a representative set of horizontal wavelengths from the medium scale to very long (λ_h = 6000 km). This choice of SCEs forms a cross in horizontal wavelength–phase speed space instead of fully covering this space. In this way we can largely reduce the number of SCEs.

[27] As discussed in detail in the following section, we determine the shape of the spectrum by launching some SCEs which are discerned only by their amplitudes, but are equal in horizontal wavelength λ_h and phase speed c_h (e.g., SCEs 7 and 9; 13 and 15; slight-phase speed differences are for technical reasons). Using intermittency factors, we can adapt the contribution of single SCEs to the total GW variance or momentum flux in order to match the observed distribution (see section 4).

4. Selection of Launch Distribution
4.1. Intermittency or Weighting Factors

[28] Intermittency factors were introduced into GW parameterization schemes in order to adjust the resulting

Table 1. Overview of Launch Parameters for All SCEs Considered in the Paper[a]

SCE no.	Figure	λ_h (km)	c_h (m s^{-1})	ampl. $\hat{u}_l$ (m s^{-1})	Experiment 0 IMF	Experiment 1 IMF	Experiment 2 IMF	Experiment 3 IMF	Experiment 4 IMF	Experiment 5 IMF
BGRD				0.5 K	5.0	5	0	0	0	0
1	2c	200	3	6.00	1.0	10	0	20	0	0
2		500	3	6.00	0.0	0	0	0	20	20
3		200	10	20.00	0.4	10	0	5	0	0
4		500	10	20.00	0.0	0	25	0	5	5
5		200	20	2.00	0.0	5	0	5	0	0
6		500	20	2.00	0.0	0	10	0	5	5
7	2d	200	30	1.00	1.0	2	0	5	0	0
8		500	30	1.00	0.0	0	0	0	5	5
9	2e	200	31	0.20	0.0	10	0	10	10	0
10		500	31	0.20	0.0	0	15	0	0	10
11		200	40	0.10	0.0	10	0	20	20	0
12		500	40	0.10	0.0	0	0	0	0	20
13	2f	200	50	0.20	0.5	2	0	0	0	0
14		500	50	0.20	0.0	0	25	0	0	0
15	2g	200	51	0.05	0.0	30	0	50	50	0
16		500	51	0.05	0.0	0	0	0	0	50
17		200	90	0.05	0.0	0	0	60	60	0
18		500	90	0.05	0.0	0	75	0	0	60
19		2000	15	2.00	0.0	0	0	30	30	30
20		1000	30	1.00	0.0	0	0	0	0	0
21		1500	30	1.00	0.0	20	10	20	20	20
22		2000	60	0.20	0.0	30	100	20	20	20
23	2h	2000	61	0.05	0.0	40	0	60	60	60
24		2000	30	1.00	1.0	20	60	20	20	20
25		3000	30	6.00	1.0	20	5	5	5	5
26		6000	30	30.00	2.0	40	0	0	0	0

[a]The panel is given for those SCEs shown in Figure 2. BGRD refers to a constant background as described for the single SCEs (see section 4.2). The different composites (Experiment 0, ..., Experiment 5) shown in Figure 3 differ in the intermittency factor (IMF) attributed to the single SCEs in generating the composite.

GW forcing of the mean background winds to the needs of the GCM [*Holton*, 1982; *Alexander and Dunkerton*, 1999; *Fritts and Alexander*, 2003]. They can be thought of as describing that GWs are intermittent in their nature and therefore not always present in the atmosphere or incompletely fill a given grid box. In this paper, we compose the spectrum of waves from single SCEs with different phase speeds and amplitudes, but always the same number of rays. In order to weight the different SCEs we introduce weighting or intermittency factors when calculating averages (e.g., zonal mean squared amplitudes). Every ray present in a considered volume (e.g., a latitude-altitude bin) is weighted by the intermittency factor of the respective SCE. This again can be thought of as describing the fact that some GWs (some SCEs) might be present more frequently or cover larger areas. Since in this paper we calculate weighted mean values (i.e., normalize to the total weight) the absolute value of the intermittency factor has no physical significance and only the relative distribution among the different SCEs influences the result (see also section 4.2).

4.2. Characteristics of Single SCEs

[29] The launch spectrum is generated from individual SCEs with respective intermittency factors in an iterative tuning process. In a first step zonal mean squared amplitudes for July from single SCEs are compared to the SABER measurements. Salient features in the distributions motivate the general composition and a first guess of suitable intermittency factors. This is described in this subsection. In a second step we vary these initial intermittency factors until the resulting composite agrees with the SABER measurements. This is discussed in following subsection (section 4.3). We have chosen July for tuning, since July distributions have a large summer-winter asymmetry. Since the southern polar vortex is stable (except in 2002), a single-day GROGRAT experiment for 15 July is sufficiently representative for tuning the wave components. Time series of the typical annual cycle discussed in section 5 then provide an independent test of the chosen launch distribution.

[30] Figure 2 compares zonal mean GW squared amplitudes for vertical wavelengths between 5 and 50 km measured by SABER (panel b) to zonal mean winds (panel a) and to the zonal means from single SCEs (panels c−i). The zonal mean zonal winds are ECMWF-TIME-GCM composites for 15 July 2003, i.e., the zonal mean of the three-dimensional global wind field used for the GROGRAT simulations. Details of the SCE launch parameters for the results shown in panels c−i are given in Table 1 together with further SCEs discussed below. For historical reasons, launch amplitudes are specified in GROGRAT as wind amplitudes in m s^{-1}. For all results shown we use squared temperature amplitudes in K^2, plotted in dB relative to 1 K^2. Average values (zonal means and, below, global maps) are calculated on a regular grid. Rays are first linearly interpolated to an altitude grid of 1 km vertical spacing. For fast waves interacting only weakly with the background atmosphere, this grid is finer than the actual calculation step. Waves which are refracted, for instance by strong vertical shear, and hence undergo larger changes in wave vector and momentum, are calculated on comparable or finer altitude steps. The vertically interpolated data are then averaged in latitude (and for global maps also longitude) bins.

[31] In order to assess the temperature perturbations induced by a single SCE at a specific altitude and latitude of a zonal cross section, we need to consider the number of rays in this latitude-altitude bin as well as the amplitude of the rays (see also Figure 4 of *Preusse et al.* [2006]). We therefore introduce a constant background of $(0.05 \text{ K})^2$. The zonal average squared amplitude $\bar{\bar{T}}^2$ is then

$$\bar{\bar{T}}^2 = \frac{1}{\sum_{i=1}^{n_z} \epsilon_i + n_l \epsilon_{bgr}} \left(\sum_{i=1}^{n_z} \epsilon_i \hat{T}_i^2 + n_l \epsilon_{bgr} (0.05 \, K)^2 \right), \quad (2)$$

where $\hat{T}_i$ are the temperature amplitudes with intermittency or weighting factors ϵ_i of all n_z rays within this latitude bin at the considered altitude and n_l is the number of rays launched in this latitude bin. Since all rays of one SCE have the same intermittency factor and the factor associated with the background is chosen the same, equation (2) simplifies to

$$\bar{\bar{T}}^2 = \frac{1}{n_z + n_l} \left(\sum_{i=1}^{n_z} \hat{T}_i^2 + n_l * (0.05 \, K)^2 \right). \quad (3)$$

[32] If, for instance, very few rays can propagate to a certain latitude or altitude ($n_z \ll n_l$), the mean value for this latitude or altitude will be close to the background (i.e., very low), and if all launched rays reach a certain latitude or altitude ($n_z = n_l$) the mean value will be the average of the background value and the average squared amplitude in this region. The background emulates that in the composite experiments there is always a mixture of different SCEs contributing to the average. A detailed motivation and discussion of the background is given in section 4.2 of *Preusse et al.* [2006]. The GROGRAT distributions shown in Figure 2 contain only data where the vertical wavelength is between 5 and 50 km and the horizontal wavelength is longer than 100 km in order to mimic the instrument visibility filter for SABER [see *Preusse et al.*, 2002, 2006].

[33] The salient features of the measured distribution in Figure 2b are a general increase in GW squared amplitudes from low to high altitudes, and high values associated with strong winds (see panel a) in the southern polar vortex and in the northern subtropics. For the subtropical maximum, convective forcing is an important source [*Preusse et al.*, 2001b; *Jiang et al.*, 2004a; *Preusse and Ern*, 2005]. At low altitudes (below 25 km) a tropical maximum is found, which extends from about 10°S to the northern subtropics. It presumably consists of long horizontal wavelength, low frequency GWs, which can only exist around the equator because their frequencies are below the Coriolis parameter limit at higher latitudes [*Alexander et al.*, 2002; *Ern et al.*, 2004; *Preusse et al.*, 2006]. Discontinuities at about 50° latitude, south and north, are caused by the yaw cycle of SABER. Around 15 July of each year SABER changes from northward viewing to southward viewing mode and the coverage alters from about 52°S–83°N to 83°S–52°N. These structures are discussed in more detail below.

[34] There is one major difference between the new SABER data shown in Figure 2b and that of the previous investigation by *Preusse et al.* [2006]. The new data exhibit a strong and monotonic increase of GW squared amplitudes above 80 km in contrast to Figure 2 in *Preusse et al.* [2006],
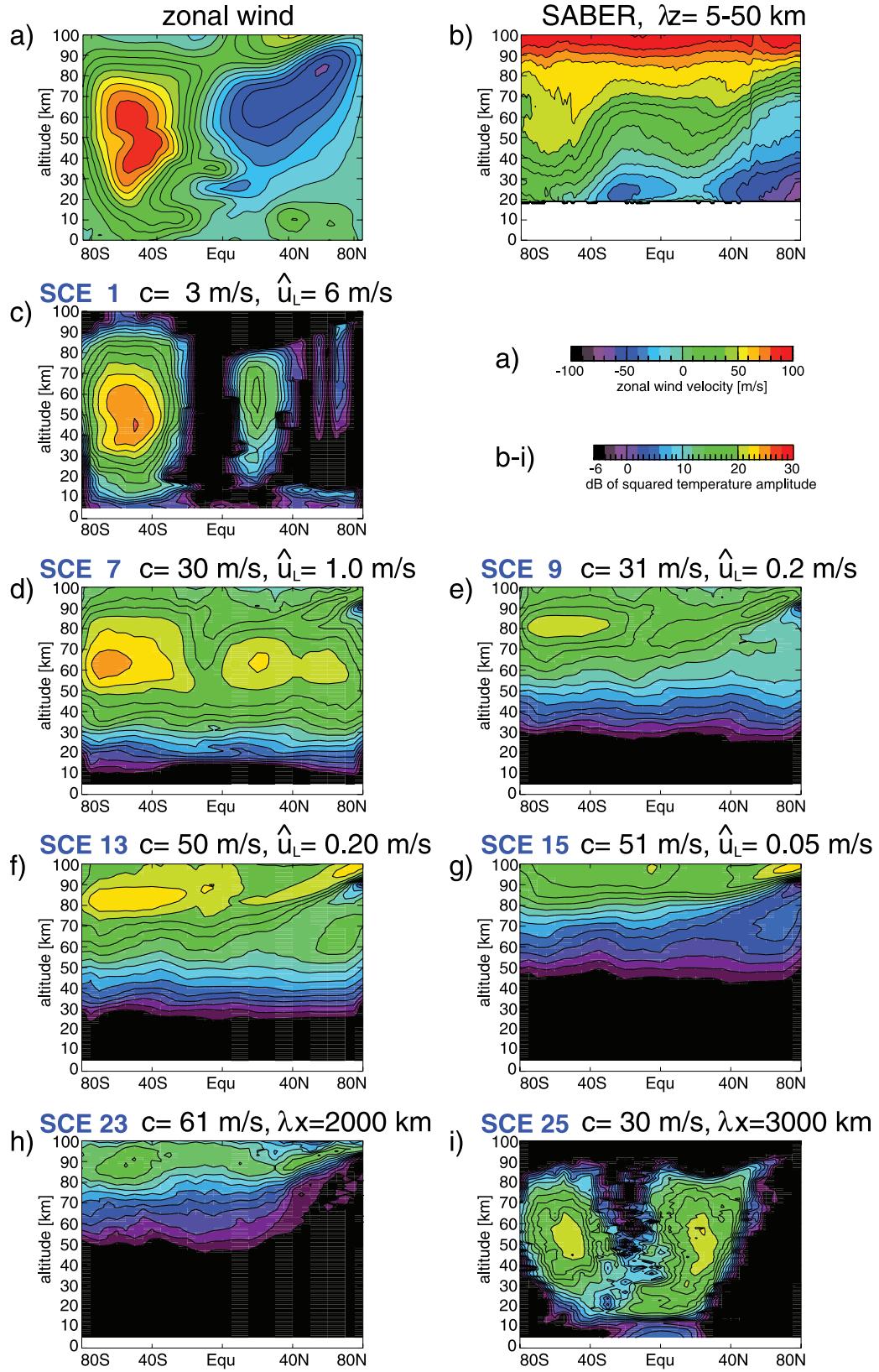
Figure 2. Comparison of July SABER GW squared amplitudes with zonal mean winds and different GROGRAT SCEs as specified in Table 1. (a) Zonal mean wind from ECMWF and TIME-GCM. (b) Average of July GW squared amplitudes deduced from SABER temperature measurements. (c–g) GROGRAT results for mesoscale waves with a 200-km horizontal wavelength and (h, i) results for long horizontal wavelength GWs. Temperature squared amplitudes are plotted in decibel relative to 1 K^2, i.e., using a logarithmic color scale. For details, see text.
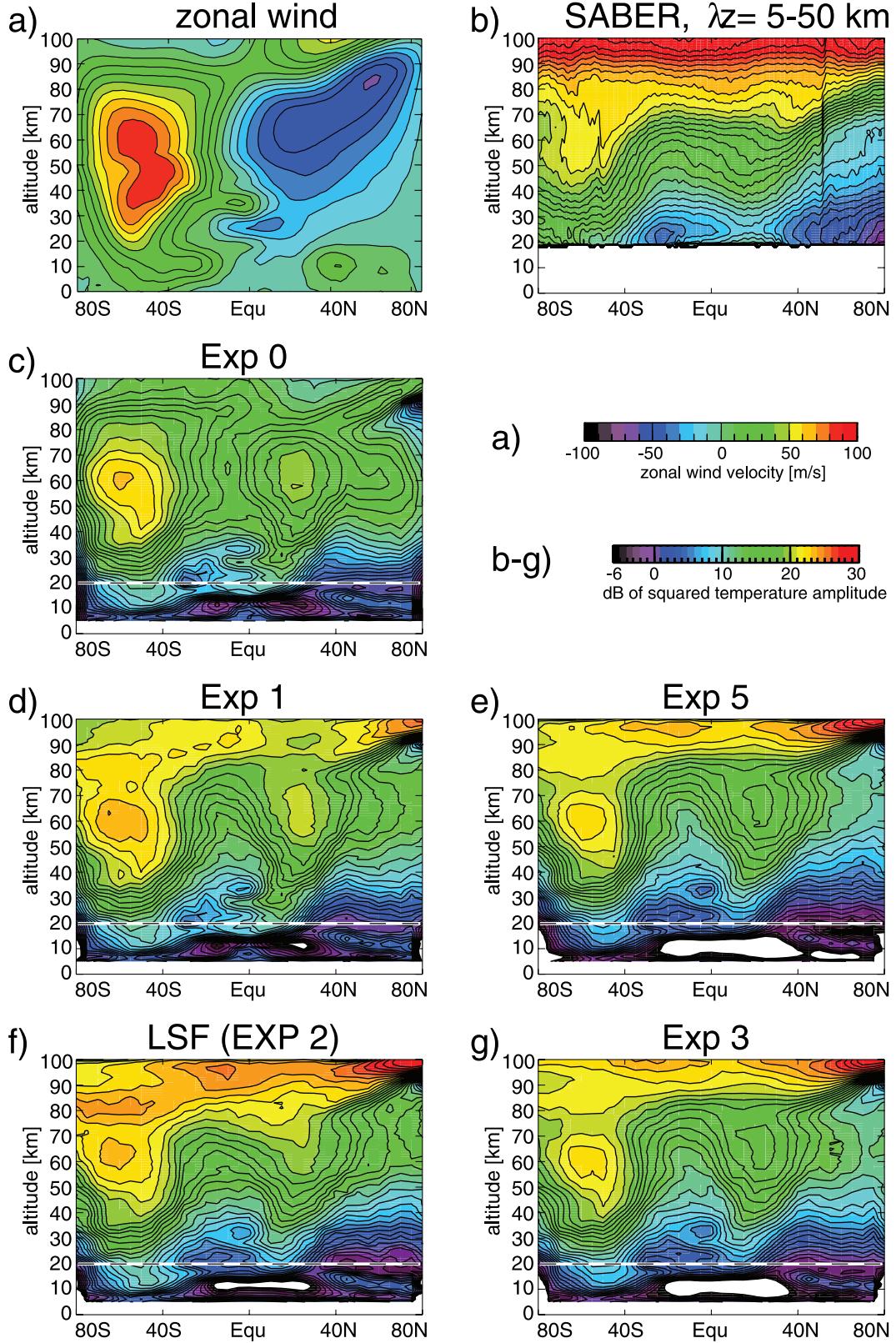
Figure 3. Comparison of July SABER GW squared amplitudes with zonal mean winds and results from different GROGRAT composite experiments. (a, b) Same as in Figure 2. (c−g) Composite experiments differ in the intermittency factors used to weigh different SCEs (see Table 1). For instance, the experiments shown in Figures 2e−2g include more fast, medium, horizontal wavelength GWs than Experiments 0 and 1 (in Figures 2c and 2d). Temperature squared amplitudes are plotted in decibel relative to 1 K^2. For details, see text.

Table 2. Relative Intermittency Factors Normalized to 1 (Total Sum of Intermittency Factors) for Four GW Categories: Slow Waves (SCE 2, 4 and 6), Medium-Fast Waves (SCE 8, 12 and 14), Very Low Amplitude Fast Waves (SCE 10, 16 and 18), and Long Horizontal Wavelength Waves (SCE 19–26)[a]

Tuning	Slow	Medium-Fast	Very Low Amplitude	Long Horizontal Wavelength
Experiment 5	0.091	0.076	0.364	0.470
July: LSF	0.108	0.077	0.277	0.538
Jan.: LSF	0.270	0.081	0.176	0.473

[a]Values are given for visual tuning (Experiment 5) and least squares optimization for July and January, respectively.

which shows a decrease of amplitude on top of the southern polar vortex. The earlier investigation was based on a previous version of the SABER temperature retrievals (Version 1.04) and focuses on waves with vertical wavelengths between 5 and 25 km. Close investigation of Version 1.04 data shows that above 65 km altitude the temperature profiles appear artificially smooth and that short vertical wavelengths are filtered out completely. The new Version 1.06 data studied in the current paper do not exhibit this artificial smoothing. In addition, here we consider a wider vertical wavelength range (5–50 km). Both effects contribute to the difference. Version 1.06 data analyzed for 5–25 km vertical wavelengths (not shown) exhibit a local maximum associated with the southern polar vortex and a slight decrease directly above (at ∼60–70 km). However, above 85 km we find a monotonic strong increase in GW squared amplitudes for the shorter vertical wavelength GWs, similar to the increase observed in Figure 2b.

[35] Figures 2c–2i show the geographical variations simulated by GROGRAT for selected SCEs. A detailed discussion of the physical reasons for the different distributions due to different phase speeds and horizontal wavelengths can be found in Appendix B and *Preusse et al.* [2006]. Briefly summarized, low-phase speed waves show strong variations due to the background winds, faster waves exhibit very little latitudinal variation and grow exponentially until they reach the saturation limit. The latitudinal distribution of long horizontal wavelength waves is additionally influenced by the Coriolis force and peaks at the equator.

[36] The saturation altitude depends on the launch amplitude. For SCE7 (panel d) saturation is reached around 50–60 km altitude, for SCE9 (panel e) saturation is reached only above 70 km. Due to this nonlinear interaction of the waves with the background winds, increasing or decreasing the wave amplitude cannot be compensated by decreasing or increasing the intermittency factor in order to obtain the same global distribution. This provides information on the launched GW spectrum: the shape of the nonsaturated part of the phase speed spectrum for the mid horizontal-wavelength GWs can be determined by launching components with different amplitudes and determining the intermittency factors from the match between measured and modeled zonal mean cross sections of temperature squared amplitudes.

4.3. Choice of Intermittency Factors

[37] Figure 2 shows that different SCEs have sufficiently different distributions to determine the intermittency factors. Examples for different composites are shown in Figure 3, the corresponding intermittency factors are listed in Table 1. Panel c (Exp 0) repeats the launch distribution deduced by *Preusse et al.* [2006]. Panels d, e and g show results of manual tuning, i.e., the intermittency factors were varied

until the best visual overall agreement is found with the observations. Panel f shows the result of minimizing the squared differences between measurements and model by variational analysis. Minimized were differences of zonal mean squared amplitudes in decibel. Using a logarithmic scale, relative deviations are minimized and hence a higher weight to the relative distributions at lower altitudes is given. This least squares approach is stable with respect to the initial choice of intermittency factors.

[38] As discussed in section 4.2 slow waves (SCE 2, 4 and 6), medium-fast waves (SCE 8, 12 and 14), very low amplitude fast waves (SCE 10, 16 and 18), and long horizontal wavelength waves (SCE 19 to 26) have clearly distinguishable global distributions. Both visual tuning and least square approach agree well in the relative distribution of the intermittency factors among these four categories as shown in Table 2. Values fitted for January are significantly different. We will come back to this point in section 5.1.

[39] Though the least squares fit provides a mathematically well defined solution, we choose to use Exp 3 and Exp 5 for further consideration because of two reasons. First, the least squares fit optimizes only for the total deviation, not for the shape of the distribution. In this way a very pronounced, unrealistic maximum is generated in the Southern Hemisphere around 80 km. Human pattern recognition is better suited than a simple mathematical measure, if not only the values but also the general shape are to be optimized. Second, additional constraints can be gained from previous investigations in the literature. For instance, high vertical resolution observations of a universal spectrum of GWs [*Fritts*, 1984; *Tsuda and Hocke*, 2002; *Fritts and Alexander*, 2003] indicate that GWs with vertical wavelengths shorter than 2–4 km in the stratosphere are saturated and accordingly we launch phase speeds below 10 m s^{-1} (SCE 1–4) saturated. In addition, horizontal wavelength and momentum flux distributions from CRISTA [*Ern et al.*, 2004, 2006], which had twice as dense horizontal sampling as SABER, can give further guidance [*Preusse et al.*, 2006].

[40] Exp 3 and Exp 5 only differ in the horizontal wavelengths of the mesoscale waves, i.e., SCEs 2, 4, … 18 with 500 km horizontal wavelength each replace SCEs 1, 3, … 17 with 200 km horizontal wavelength, respectively. Figure 3 shows that these two experiments are almost indistinguishable in terms of GW squared amplitudes. Therefore we need additional data to constrain the horizontal wavelength and compare absolute values of momentum flux from the ray tracing experiments to CRISTA momentum flux estimates.

4.4. Horizontal Wavelength and Momentum Flux Constraints

[41] CRISTA took measurements during two 1-week periods in October 1994 (CRISTA-1) and August 1997

(CRISTA-2) [*Offermann et al.*, 1999; *Riese et al.*, 1999; *Grossmann et al.*, 2002]. Both missions have been analyzed for absolute values of GW momentum flux [*Ern et al.*, 2006]. The inferred momentum flux values well agree with measurements from long-duration balloons over Antarctica [*Hertzog et al.*, 2008].

[42] Momentum flux can be inferred from temperature variations by equation (7) of *Ern et al.* [2004] if both the horizontal wavelength and the vertical wavelength of the wave are known:

$$|F_{ph}| = \frac{1}{2}\rho\left|\frac{k_h}{m}\right|\left(\frac{g}{N}\right)^2\left(\frac{\hat{T}}{T}\right)^2, \qquad (4)$$

where $k_h = 2\pi/\lambda_h$ is the horizontal wave number, $m = 2\pi/\lambda_z$ is the vertical wave number, $\hat{T}$ is the temperature amplitude, and ρ, N and T are density, buoyancy frequency and temperature of the background atmosphere. The horizontal sampling distance of CRISTA was ~200 km, which implies a Nyquist wavelength (i.e., shortest resolvable wavelength) of 400 km. *Ern et al.* [2004] showed that CRISTA data undersample the measured GWs and that some effects of aliasing occur when inferring horizontal wavelength distributions. The horizontal sampling distance of SABER is twice as large as the CRISTA sampling distance and therefore too coarse to retrieve horizontal wavelengths and thus momentum flux estimates for GWs.

[43] Figure 4 compares absolute values of GW momentum flux in dB relative to 1 Pa measured by CRISTA-2 (Aug. 1997, panel a) and CRISTA-1 (November 1994, panel e) with GROGRAT results for Exp. 3 (b, f), Exp. 4 (c, g) and Exp. 5 (d, h) calculated for 15 Aug. 2003 (b–d) and 15 November 2003 (f–h). The difference among the three composites is the horizontal wavelength distribution. Experiment 3 uses $\lambda_h = 200$ km for all mesoscale components, Exp. 4 uses $\lambda_h = 200$ km for the fast waves and $\lambda_h = 500$ km for the slow waves, which dominate the lower altitudes, and Exp. 5 uses $\lambda_h = 500$ km for all mesoscale components. An observational filter of $\lambda_z = [5, 20]$ km is applied to the GROGRAT results. Note that due to the observational filter GW momentum flux can increase with increasing altitude. This is observed, for instance, at the summer polar mesopause. Although the momentum flux of each individual wave remains constant or decreases with altitude, increases with height are possible because some waves carrying large GW momentum flux are refracted in vertical wavelengths, shift into the range of the observational filter, and become visible in the zonal means.

[44] From equation (4) we expect the 500 km horizontal wavelength waves to carry a fraction of 2/5 of the momentum flux of the 200 km waves, which corresponds to an offset of ~4 dB in Figure 4. In agreement with *Preusse et al.* [2006], we find that momentum flux distributions based on a typical wavelength of 500 km for the mesoscale waves match the observations well, whereas assuming a typical wavelength of 200 km overestimates the GW momentum flux. Experiment 4, which combines 500 km horizontal wavelength for the slower and 200 km horizontal wavelength for the faster mesoscale SCEs (see Table 1), is very similar to Exp. 5 in the stratosphere. This means that the horizontal wavelengths of the very fast waves with small launch amplitudes cannot be sufficiently constrained by the CRISTA stratospheric observations.

[45] Overall, given both GW squared amplitudes and momentum flux, Exp. 5 matches the observations best. GW squared amplitudes show low values in the summer hemisphere and tilted isolines at a similar angle as the observations, reasonably high values at the equator and a monotonic increase in the upper mesosphere. The momentum flux values compare favorable with the CRISTA measurements. We therefore choose Exp. 5 for further discussion.

5. Annual Cycle in SABER and GROGRAT GW Results

5.1. Global Maps in Lower Stratosphere

[46] SABER: Figure 5 shows global maps at 28 km altitude of GW squared temperature amplitudes of the largest amplitude wave component for vertical wavelengths between 5 km and 50 km. The data are binned to a 1° latitude × 2° longitude grid using a triangular weight of 800 km width, i.e., a SABER point is weighted 1 if it coincides with a grid point, weighted zero if the distance between SABER point and grid point is larger than 800 km, and weighted with a linearly interpolated value between 0 and 1 for distances in between.

[47] The resulting maps for the two solstices (January and July) are essentially mirror images with respect to the equator and are both very different from the two maps at equinox (April and October). At the solstices a very pronounced winter vortex maximum is the dominant feature and a secondary maximum can be found in the tropics and subtropics of the summer hemisphere. The GW variances at high summer latitudes are very low. These are all features well known from GW temperature variances extracted from a number of different satellite instruments [*Wu and Waters*, 1997; *Ern et al.*, 2004, 2006; *de la Torre et al.*, 2006; *Wu and Eckermann*, 2008]. The summer low latitude maximum is commonly attributed to convectively generated GWs in the monsoon regions and above high sea surface temperature regions and correlates well with convection proxies [*McLandress et al.*, 2000; *Preusse et al.*, 2001b; *Jiang et al.*, 2004a; *Preusse and Ern*, 2005]. The comparison of July and August values shows that the most active region in Asia shifts eastward from the Indian monsoon toward the Kuro-

Figure 4. Comparison of measured absolute values of GW momentum flux by (a) CRISTA-2 (August 1997) and (e) CRISTA-1 (November 1994) with absolute values of momentum flux for (b, f) Experiment 3, (c, g), Experiment 4, and (d, h) Experiment 5 calculated for (b–d) 15 August 2003 and (f–h) 15 November 2003. Horizontal dashed lines in the GROGRAT simulations indicate the altitude range of the CRISTA results. The three composites differ in the launch distribution of horizontal wavelengths. Experiment 3 uses $\lambda_h = 200$ km for all mesoscale components, Experiment 4 uses $\lambda_h = 200$ km for the fast waves and $\lambda_h = 500$ km for the slow waves dominating the lower altitudes, and Experiment 5 uses $\lambda_h = 500$ km for all mesoscale components. For discussion, see text.
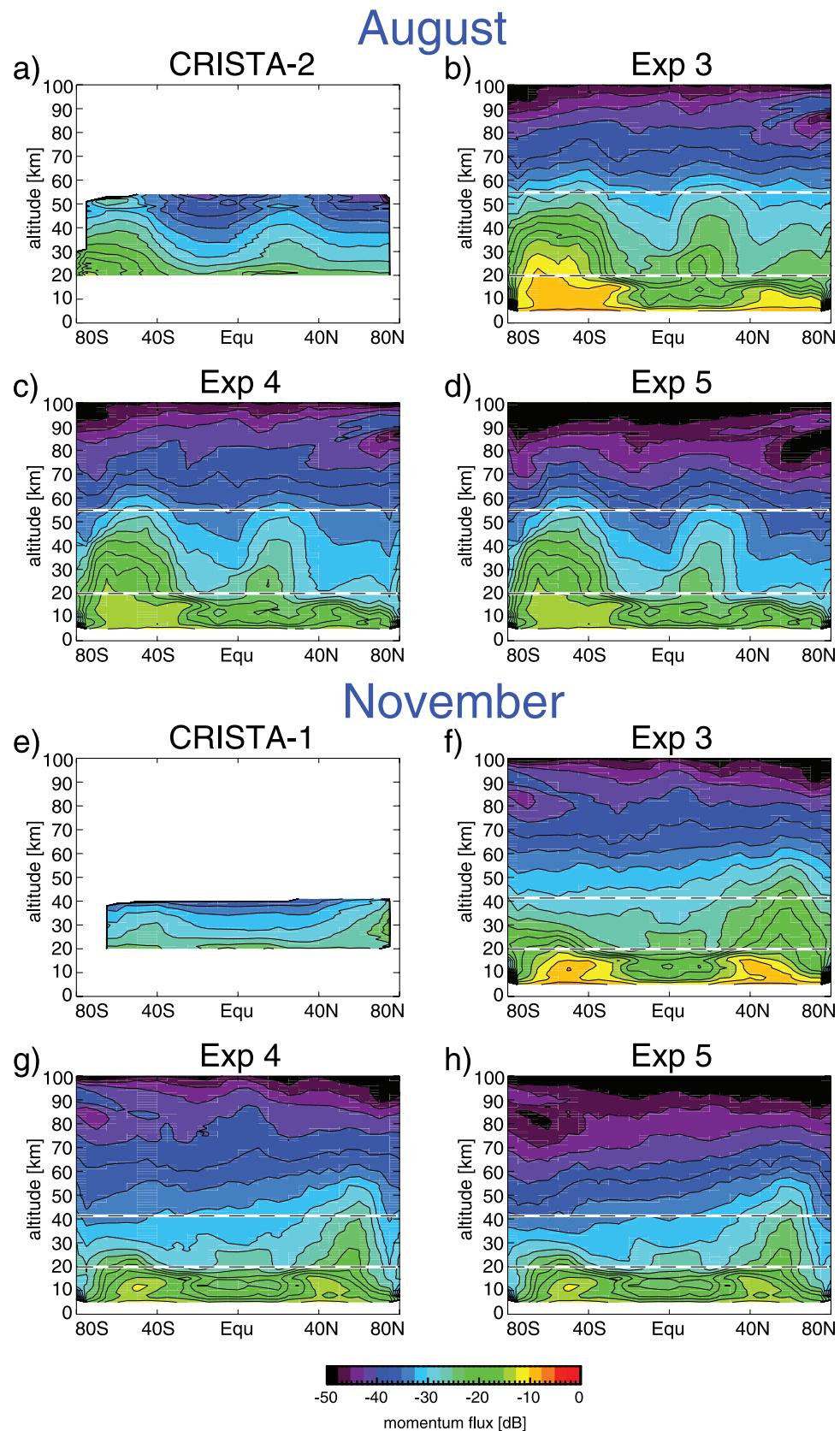
Figure 4
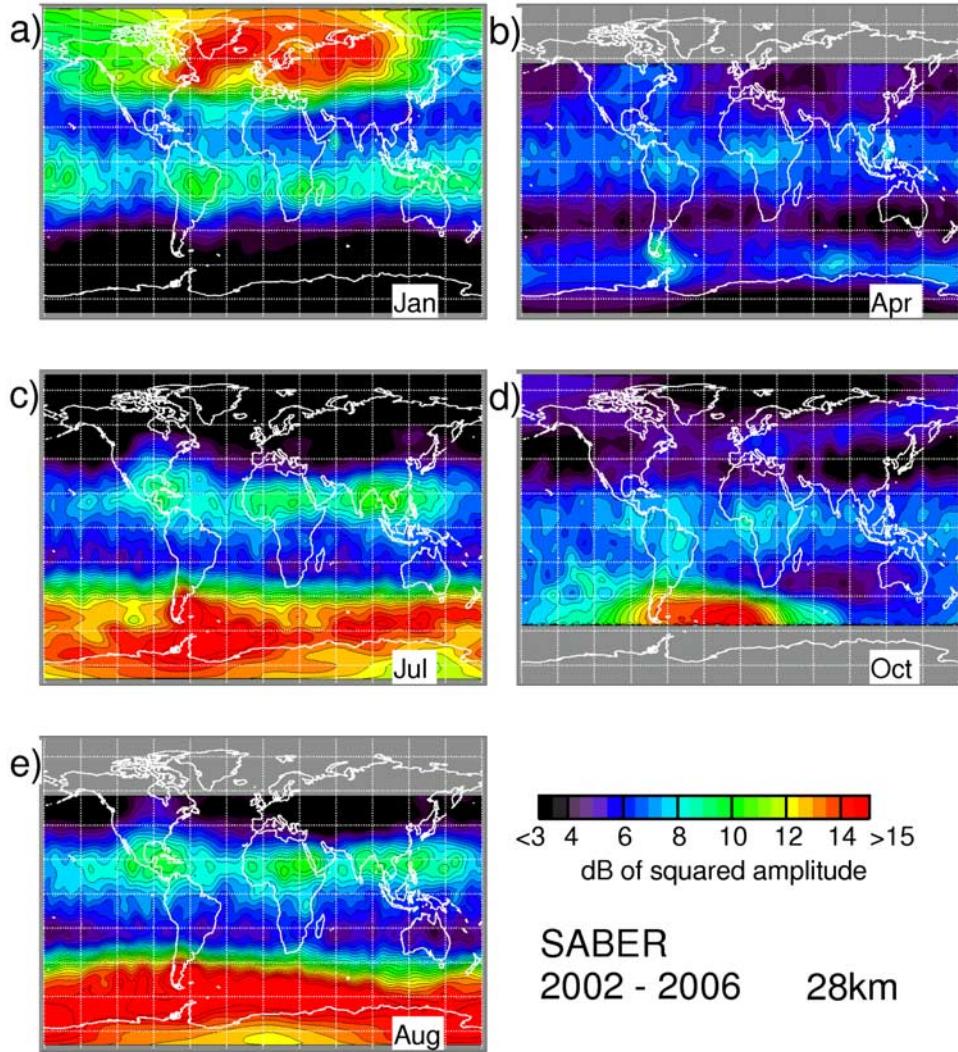
Figure 5. Global maps of SABER GW squared amplitudes for vertical wavelengths from 5 to 50 km at a 28-km altitude. Values are binned according to calendar month for the time period February 2002– December 2006.

Shio ocean stream. This more eastward position of subtropical wave activity is very similar to the CRISTA observations [*Preusse et al.*, 2001b; *Ern et al.*, 2004] and is connected with a further northward shift into the subtropics. It should also be noted that high GW momentum flux in the summer subtropics was explained, at least to some extent, by wind filtering [*Ern et al.*, 2004].

[48] There are two noticeable differences between the two respective hemispheres. First, during solstices the wave activity in the winter vortex is stronger and much more zonally symmetric in the Southern Hemisphere (SH) due to a more stable winter polar vortex and weaker planetary wave activity. Second, the subtropical band of high wave activity extends further northward in July than southward in January, which might be due to a more pronounced monsoon season in the Northern Hemisphere (NH).

[49] At the equinoxes, tropical GW variances are symmetric about the equator and much less pronounced than at the solstices. At higher latitudes wave activity is often found over regions where orography could contribute to the forcing: for instance above the southern tip of South America and the Eurasian continent. This agrees with previous studies by *Eckermann and Preusse* [1999] and *Jiang et al.* [2002, 2004b] modeling GW activity found in CRISTA and MLS data with the NRL mountain wave forecast model (NRL-MWFM).

[50] GROGRAT: Figure 6 shows global maps at 28 km altitude of GROGRAT GW squared temperature amplitudes from Exp. 5 for vertical wavelengths from 5 km to 50 km. The ray traces are calculated for background atmospheres for 00 GMT on days 3, 6, 9, . . ., and 27 of the respective month in 2003 and 2004. This provides a sufficiently large database to obtain a representative average of meteorological situations including different phases of the QBO. Highly variable tropospheric weather conditions average out, but the preferential phase of the strong quasistationary planetary waves in the northern winter is a persistent feature.

[51] It should kept in mind, however, that the GROGRAT modeling assumes a homogeneous and isotropic GW source
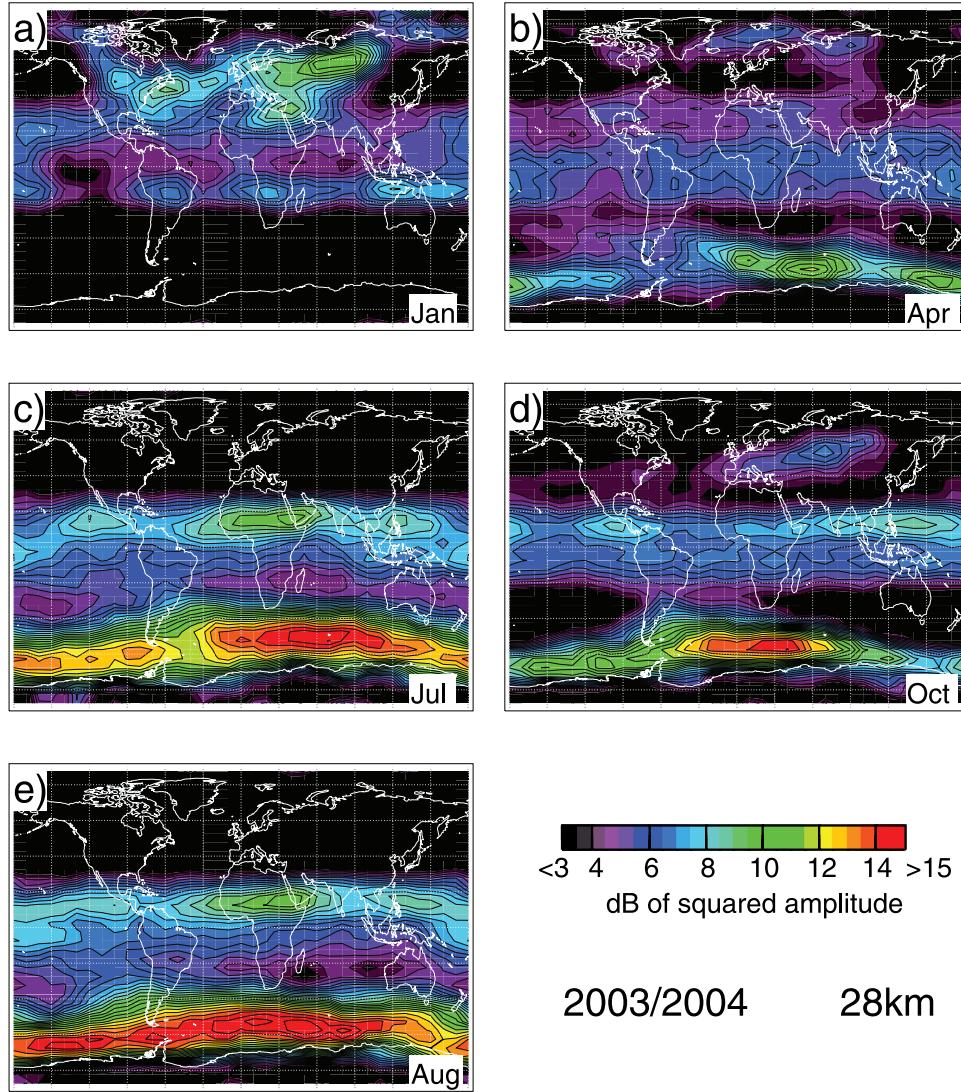
Figure 6. Global maps for 28-km altitude of GROGRAT GW squared temperature amplitudes from composite Experiment 5 for vertical wavelengths from 5 to 50 km. For details, see text.

and therefore does not include strong localized GW sources such as orography or deep convection.

[52] The modeled fields reproduce the observations in many respects, such as the asymmetry between northern and Southern Hemisphere with respect to the polar vortex and the absence/presence of strong planetary waves modulating the GW activity in the polar vortex. The lower wave activity in the GROGRAT results at very high southern latitudes could be due to the latitudinal boundary in the model. This would have to be reinvestigated with a launch distribution extending to the pole and with a model version allowing cross-pole propagation. The model results also reproduce the shift of GW activity into the summer hemisphere in the tropics and the symmetry with respect to the equator for the equinoxes. In addition, the simulated seasonal cycle of GW squared amplitudes in the southern polar vortex is quite realistic: an absence of wave activity in January; the buildup of the vortex wave activity in April; strong, almost zonally symmetric wave activity in July; and a decaying vortex disturbed by planetary waves in October. In January measurement and model agree in the

position of the high latitude maxima of GW squared amplitudes above eastern Europe and central Asia (30°E–90°E) and at the east coast of North America. The position of the maxima reflects the preferential phase of the planetary waves and hence the position of the vortex edge in the Northern Hemisphere winter.

[53] However, for Northern Hemisphere winter the magnitude of GW activity in the model is much smaller than in the observations and the model exhibits a much stronger asymmetry between southern and Northern Hemisphere winter polar vortex values than the measurements, which show essentially equal peak values for the Southern Hemisphere in July and the Northern Hemisphere in January. Weaker winds in the Northern Hemisphere result in weaker GW activity for the model results in particular by slow, saturated GWs. In the measurements this is likely compensated by orographic forcing by the more numerous mountain ranges in the Northern Hemisphere, for instance the south tip of Greenland, the Norwegian mountain ridge, the Alps, and the Urals,
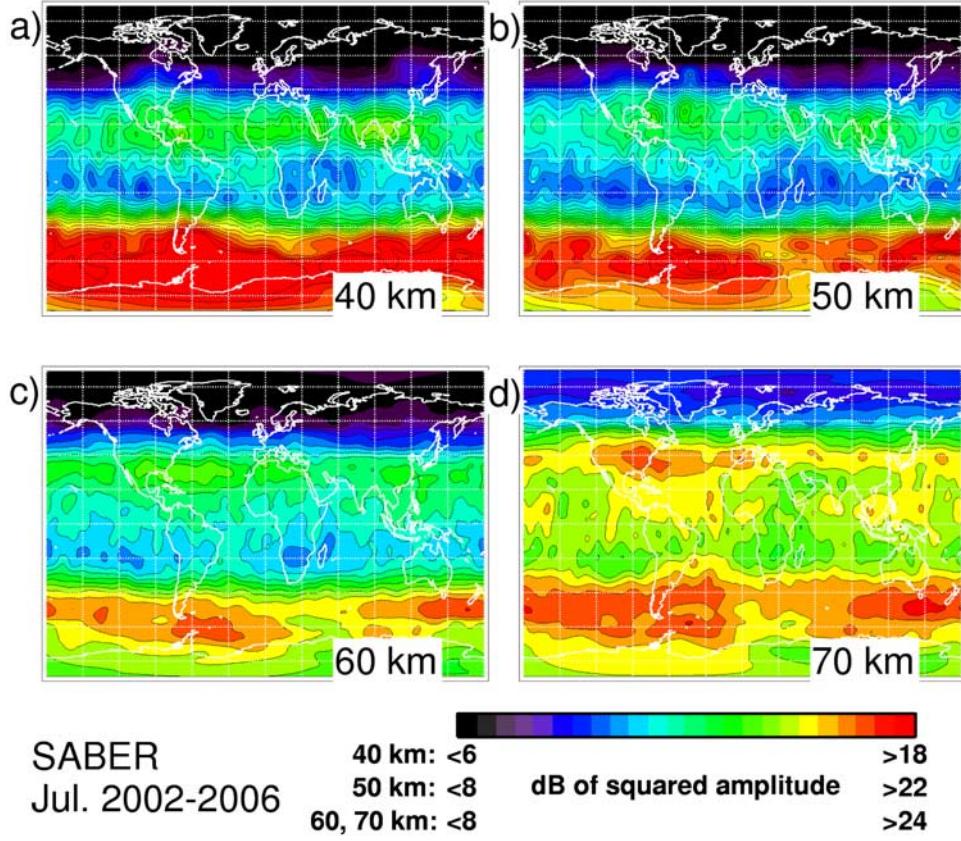
Figure 7. Same as Figure 5c, but for altitudes of 40, 50, 60, and 70 km.

which are all prominent sources of stratospheric GWs [*Eckermann and Preusse*, 1999; *Dörnbrack and Leutbecher*, 2001; *Jiang et al.*, 2004b]. This explanation is supported by the results of the least squares method for January in Table 2: For January we find more than twice as large intermittency factors for slow-phase speed waves than in July. Interestingly, even in this 5 year climatology we do not find enhanced amplitudes above the Rocky Mountains, which is in agreement with previous studies [*Eckermann and Preusse*, 1999; *Jiang et al.*, 2004b]. In contrast to the Northern Hemisphere, orography is responsible only for a small fraction of the waves observed in the SH winter; that is orographically forced waves above the south tip of South America and the Antarctic Peninsula [*Eckermann and Preusse*, 1999; *Jiang et al.*, 2002; *Ern et al.*, 2006].

[54] Furthermore, the high GW squared amplitudes over the Gulf of Mexico and the Asian monsoon regions are not reproduced, indicating that these are features generated primarily by convective sources rather than by the modulation of GWs by the background winds [see discussion of the SABER maps in *McLandress et al.*, 2000; *Preusse et al.*, 2001b; *Jiang et al.*, 2004a; *Ern et al.*, 2004; *Preusse and Ern*, 2005]. The same likely applies for the observed enhanced GW activity in the tropics/subtropics in January, which is not reproduced by the model (there is a southward shift, but no real enhancement in Figure 6a).

5.2. July Maps in Stratosphere and Mesosphere

[55] SABER: Figure 7 shows GW squared amplitudes in July, same as Figure 5c, but for altitudes from 40 km to 70 km. At 40 km altitude we find the same subtropical maxima as for 28 km altitude in Figure 5c. These local maxima are somewhat less pronounced with respect to the background GW variances at 50 km, but still noticeable. At 60 km and 70 km altitude, however, the subtropical maximum becomes more band-like (i.e., zonally symmetric) and is shifted further to the north. There are two likely explanations for this behavior. First, as altitude increases waves propagate further away from their sources horizontally. Variance enhancements due to localized sources therefore smear out with increasing altitude. Second, as waves propagate upward, smaller amplitude waves with less pronounced sources or from a GW background can grow more strongly than waves forced with larger amplitudes closer to the saturation limit, so at higher altitudes they gain comparable amplitudes. The influence of the wind fields by critical level filtering, wind modulation and visibility filter [*Preusse et al.*, 2006] therefore becomes more important for the horizontal distribution than the influence of the sources at higher altitudes.

[56] GROGRAT: At higher altitudes the simulated GROGRAT amplitudes still largely resembles the observations as can be seen from Figure 8. The absolute values at the respective altitudes and the relative strength of the southern polar vortex and the northern subtropical maximum agree well with the SABER results in Figure 7. Of course, these source-invariant GROGRAT simulations can neither reproduce the convectively forced GWs above Florida and the Asian Monsoon regions nor the loss of these features with altitude. Further, a general underestimate
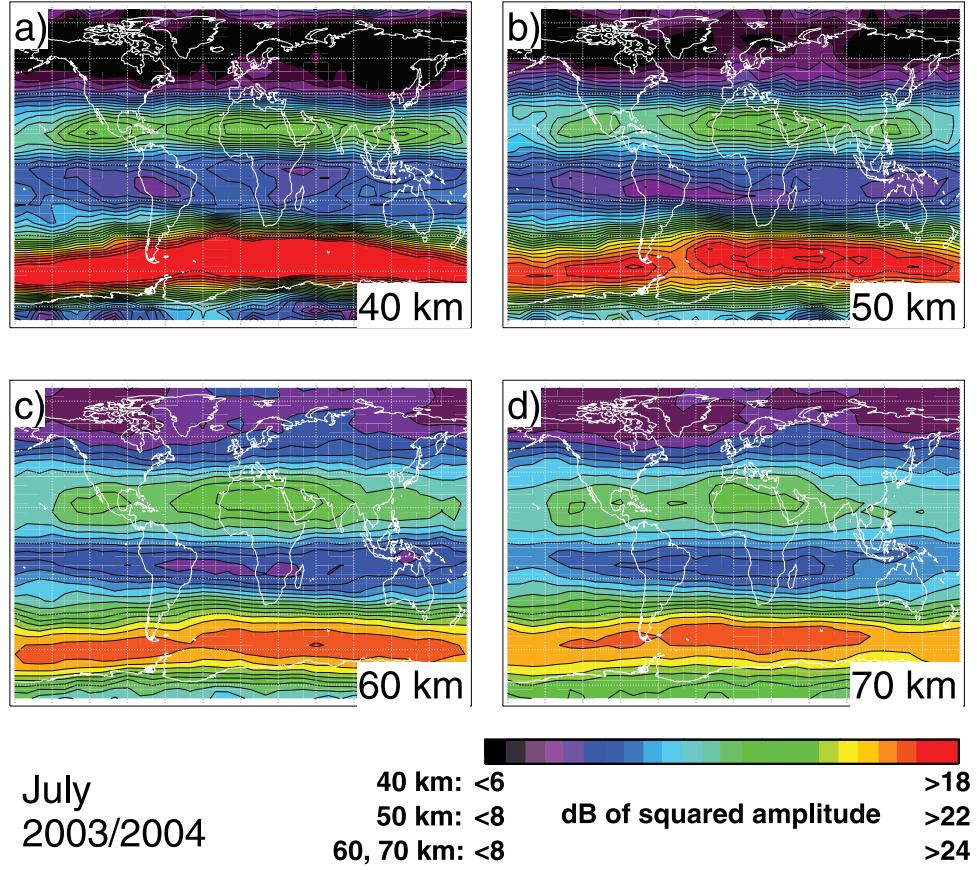
Figure 8. Same as Figure 6, but for July and altitudes of 40, 50, 60, and 70 km.

of GW squared amplitudes in the southern subtropics points to a dilemma of either overestimating the high summer latitudes or underestimating the tropical and subtropical values of the winter hemisphere. The GROGRAT results without the vertical wavelength visibility filter applied (not shown) are very similar in their global distributions and only have an offset of less than 1 dB. This indicates that critical level filtering and wind modulation are the dominant processes in shaping the distributions observed by SABER (Figure 7).

5.3. Time Series of Zonal Mean Squared Amplitudes

[57] Figure 9 compares time series of zonal mean squared GW amplitudes measured by SABER (left column) with the results from GROGRAT Exp. 5 (right column). As for the maps (see section 5.1), the zonal means are averages of GROGRAT results calculated for every third day of the respective months in 2003 and 2004. Results at altitudes between 30 km and 90 km are shown and observed and modeled structures agree in their salient features.

[58] At 30 km altitude, SABER observes high GW squared amplitudes in the winter polar vortices. They contrast with very low GW activity in the summer mid and high latitudes. In the tropics and subtropics, the phase of the annual cycle is reversed and maxima for the SABER measurements are found after the summer solstice, i.e., values are maximum in July and August in the Northern Hemisphere and maximum in January and February in the Southern Hemisphere. The high latitude maxima shift to

early winter at 50 km altitude whereas the subtropical maximum remains fixed in time. This is in agreement with Figure 2f of *Krebsbach and Preusse* [2007], which shows the altitude-latitude variations of the maximum of the annual cycle deduced from SABER GW analyses. *Krebsbach and Preusse* [2007] find a downward progression of the phase (time) of the high latitude wave-variance maximum in the polar vortices but an almost constant phase of the subtropical maximum throughout the entire stratosphere.

[59] The GROGRAT modeling reproduces the enhanced wave amplitudes in the winter polar vortices well, and also the shift toward earlier months at increasing altitude. The hemispheric asymmetry between the very large GW squared amplitudes in the Southern Hemisphere winter polar vortex and the somewhat weaker values in the Northern Hemisphere winter polar vortex is even more pronounced in the GROGRAT model results. As discussed in section 5.1, a potential explanation is that the GROGRAT simulation does not take into account the enhanced forcing of GWs by orography in the Northern Hemisphere relative to the Southern Hemisphere.

[60] The subtropical maximum is less pronounced in the GROGRAT modeling than in the observations. The difference further supports the assumption that the observed maxima are caused to a large extent by convection during the monsoon and above regions of high sea surface temperature (SST), as has been found from correlations of GWs to cloud proxies and SST [*McLandress et al.*, 2000; *Preusse*
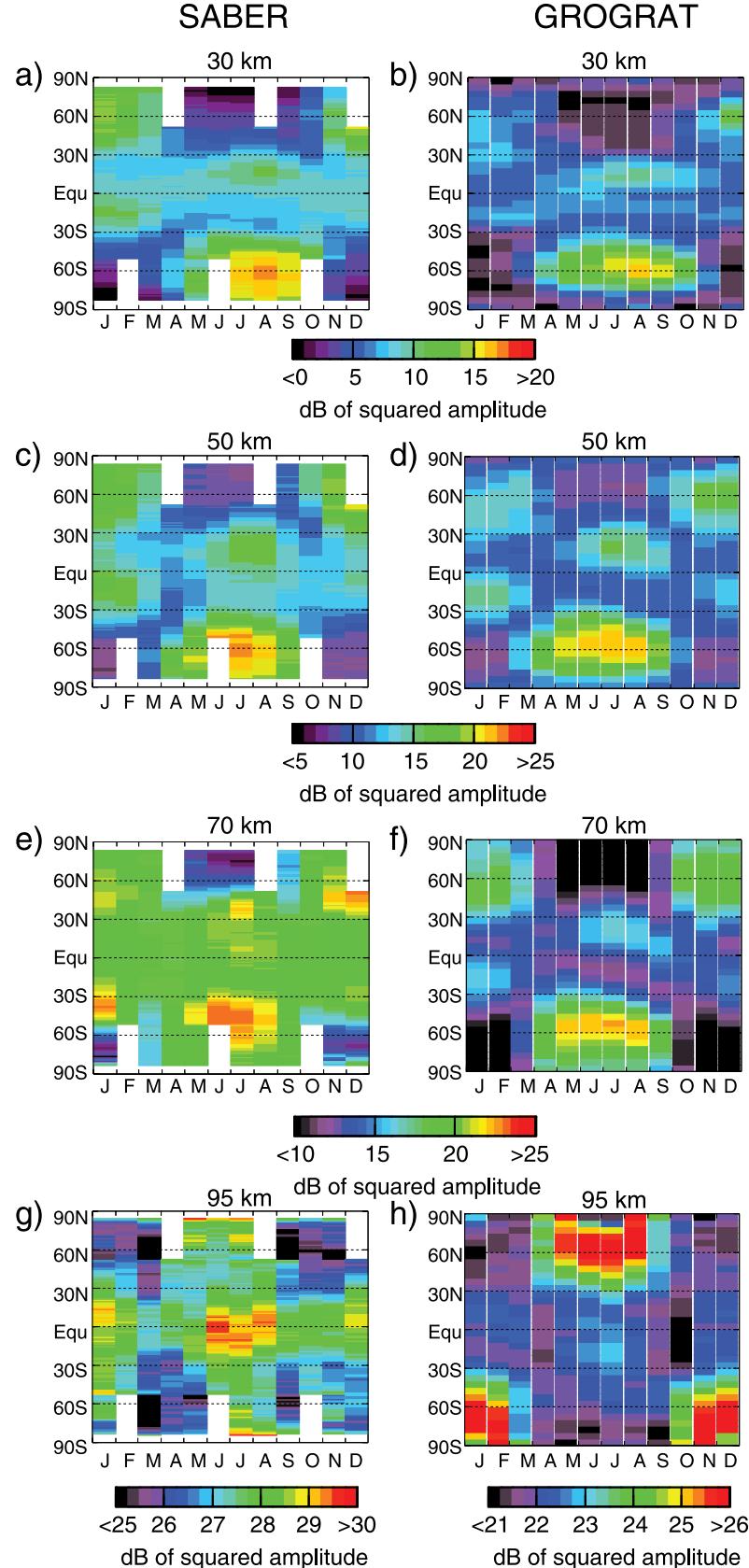
Figure 9. Time series of zonal mean GW squared amplitudes. (left) SABER values are monthly averages combining data from 2002 to 2006. (right) GROGRAT values from Experiment 5 are calculated from every third day of each month in 2003 and 2004. Color scales are the same for SABER and GROGRAT results for the respective altitudes of 30, 40, 70, and 95 km. See text for further discussion.
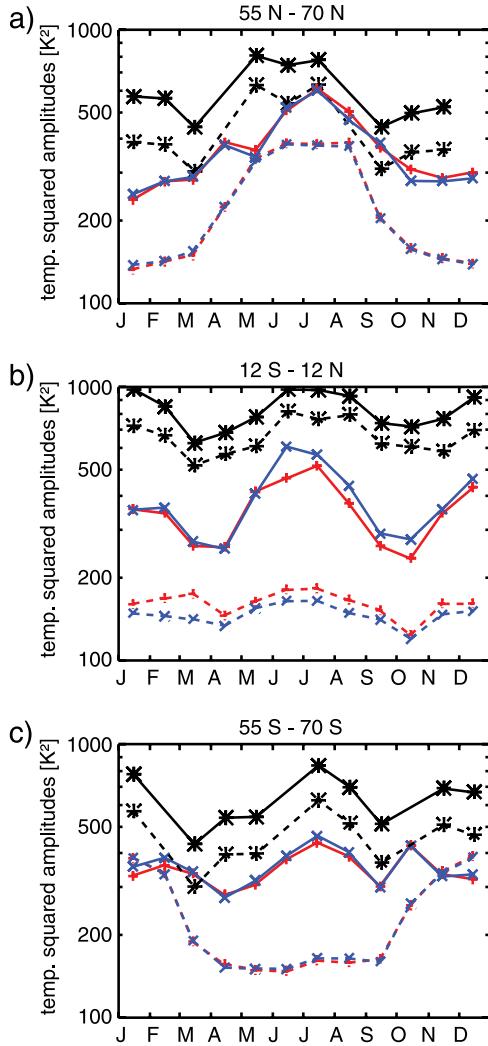
Figure 10. Time series of (red) GROGRAT model results for 00 GMT, (blue) GROGRAT model results for 12 GMT, and (black) SABER data at (dashed) 95-km and (solid) 100-km altitudes for (a) northern midlatitudes and high latitudes, (b) the tropics, and (c) southern midlatitudes and high latitudes. GROGRAT underestimates the SABER results by about a factor of 2−4, but the annual variation is well reproduced, except for the Southern Hemisphere, 95 km.

et al., 2001b; *Jiang et al.*, 2004a; *Ern et al.*, 2004; *Preusse and Ern*, 2005].

[61] At 70 km altitude (Figures 9e and 9f) the summertime subtropical maxima extend further poleward and the maxima associated with the polar vortex extend further equatorward. At 30−40° latitude this yields to a clear semiannual variation of GW variances with peaks at the solstices, in general agreement with radar measurements of gravity wave wind variances in this latitude and height vicinity [*Vincent and Fritts*, 1987; *Thorsen and Franke*, 1998; *Gavrilov et al.*, 2000]. The GROGRAT results reproduce semiannual variability at these latitudes, but with a stronger annual component. We will discuss this feature in more detail in section 6.

[62] At 95 km altitude the GROGRAT model results underestimate the SABER values by about 4−6 dB. The

most interesting feature in both measurements and model results is a high latitude summer maximum in the Northern Hemisphere. The SABER feature is particularly interesting since ground-based radar data at high latitudes [*Dowdy et al.*, 2007] show a semiannual variation at 80 km and winter maxima at 90 km for shorter period waves (<120 minutes [*Dowdy et al.*, 2007, Figure 7]) and a mixture of semiannual and annual variation at both altitudes, but strongly dependent on location, for longer period waves (120−480 minutes [*Dowdy et al.*, 2007, Figure 8]). Similar results are also reported by *Beldon and Mitchell* [2009]. This suggests that the seasonal variation at these altitudes differs for different parts of the GW spectrum and that SABER sees different waves than both spectral windows of the radar measurements.

[63] In the south, SABER shows a more semiannual variation with similar peaks in summer and winter, whereas GROGRAT produces a summer maximum like for the Northern Hemisphere. In the south, SABER shows a more semiannual variation with similar peaks in summer and winter, whereas GROGRAT produces a summer maximum like for the Northern Hemisphere. Figure 10 investigates the annual cycle for high altitudes more closely. Shown are temperature squared amplitudes for 95 km and 100 km altitude from SABER and GROGRAT on logarithmic scale. GROGRAT values are in general a factor 2−4 lower, corresponding to 3−6 dB in Figure 9. In the Northern Hemisphere at both altitudes a summer maximum is observed in the GROGRAT results, in the Southern Hemisphere there is a summer maximum at 95 km altitude, but a semiannual variation at 100 km altitude. This shows that the annual variation of the GROGRAT results in the Southern Hemisphere has a very complex altitude dependence. Slight mismatches of observed and modeled winds could therefore be responsible for the differences. In addition, the annual cycle at high altitudes is sensitive to the composition of the spectrum.

[64] We have compared annual cycles at 80 and 95 km altitude for slow and fast mesoscale GWs as well as fast long horizontal wavelength waves. The results show that very slow GWs are filtered out and that phase speeds around $c = 30$ m s^{-1} are strongly reduced in amplitude, but retain a winter maximum. Long horizontal wavelength waves also have a winter maximum at both altitudes. Only fast-phase speed, mesoscale waves (SCEs 16 and 18; $c = 51$ m s^{-1} and $c = 90$ m s^{-1}) reproduce the reversal of the annual cycle between 80 and 95 km altitude.

[65] All our model results are based on the general assumption of a homogeneous, isotropic and temporal constant launch spectrum in the troposphere. At higher altitudes waves can be only removed, but no new waves are launched. Both contrasts to our general understanding of GW sources. We assume GWs to be generated by orography, convection or spontaneous adjustment, all localized processes. At higher altitudes secondary waves are forced when GWs propagating upward from lower altitudes break. In addition, the launch spectrum is simplified and only a limited number of SCEs is calculated.

[66] Despite these facts both, global maps at different seasons and the annual cycle, are reasonably well reproduced at all altitudes. This is an independent test of the launch distribution, since only July zonal mean values were
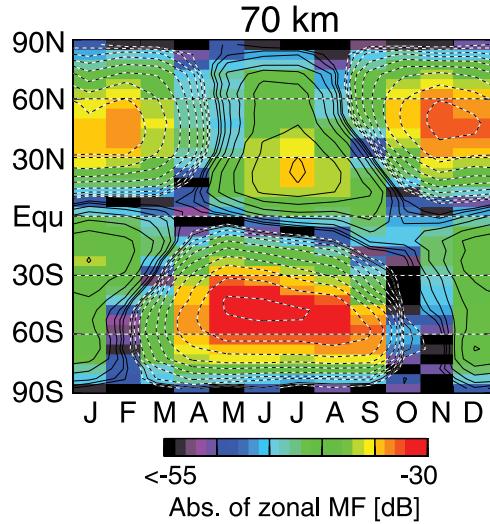
Figure 11. Time series of zonal momentum flux for composite 5 at 70-km altitude. Color code gives the absolute value of zonal GW momentum flux given in decibel over 1 Pa; contour lines show direction: solid contours indicate positive values, i.e., preferentially eastward propagation, dashed contours indicate negative values, i.e., preferentially westward propagation.

used for the tuning. In particular, at high altitudes the seasonal cycle depends on the composition of the launch spectrum. For the Northern Hemisphere and the tropics both magnitude as well as phase of the variations observed by SABER are matched by the model results. In the Southern Hemisphere the annual cycle in the model results shows a complex altitude structure. Accordingly, there are deviations around 95 km, but good agreement again at 100 km altitude.

[67] The overall agreement therefore indicates that the intermittency factors have been tuned to broadly realistic values.

6. Propagation Direction and Distance, Momentum Flux, and Mean Flow Acceleration

[68] As pointed out in section 4, the choice of wave components and intermittency factors is based only on tuning to boreal summer results. In section 5, the annual cycle of GW squared amplitudes from SABER therefore provides an independent observation to test the adequacy of the resulting simulations. The good agreement found between observations and model results supports the choice of SCEs and intermittency factors deduced from boreal summer observations. Though there are still deviations between the observations and the model results, probably mainly due to missing GW sources, we have now gained sufficient confidence in the model results that we can infer quantities which cannot be measured directly.

6.1. Time Series of Zonal Propagation Direction

[69] An open question is the nature of the strong midlatitude semiannual variation in GW squared amplitudes found in the mesosphere. *Krebsbach and Preusse* [2007] spectrally analyzed a 4-year data series of root mean square (RMS) zonal averages. Around 70 km they found about 2.0–2.5 K

semiannual amplitude for 40° latitude in both hemispheres, but only 0.5–1.0 K semiannual amplitude in the tropics where we expect to find modulation of GWs by the well-known mesospheric semiannual oscillation (SAO) in the tropical zonal winds [*Hirota*, 1978; *Burrage et al.*, 1996]. *Krebsbach and Preusse* [2007] speculated that the variations at 40° latitude are not SAO signals but rather an annual cycle, if GW momentum flux and, in particular, its direction is considered.

[70] The general argument can be understood by reconsidering the altitude evolution of the annual cycle shown in Figure 9. At 30 km and 50 km altitude (Figures 9a and 9c) there is a subtropical summer maximum southward of 30°N and a mid and high latitude winter maximum northward of 30°N. For the summer maximum we expect preferential eastward propagation opposite to easterly background winds and for the winter maximum we expect preferential westward propagation opposite to westerly background winds. At 70 km altitude (Figure 9e) the GW activity related to the polar vortex spreads equatorward and the subtropical maximum spreads poleward to overlap between 25°N and 50°N. The two maxima result in a semiannual component, however since we expect opposite preferential propagation directions the momentum flux points in opposite directions and for momentum flux we would observe an annual cycle. We test this hypothesis by calculating the average zonal momentum flux from the GROGRAT simulations, which is shown in Figure 11.

[71] The color scale in Figure 11 indicates the absolute value of the zonal momentum flux, overplotted solid lines indicate positive values, i.e., preferentially eastward propagating waves, overplotted dashed lines indicate negative values, i.e., preferentially westward propagating waves. As expected, waves propagate preferentially eastward against the subtropical easterly jet in the summer of the respective hemisphere and preferentially westward against the polar vortex jet in winter. At the equinoxes, the average zonal momentum flux vanishes. Figures 9e and 9f still show significant GW activity at these times, i.e., the vanishing zonal momentum flux is caused by flux cancellation caused by GWs propagating in different directions rather than by an absence of waves. This interpretation is supported by ground-based radar measurements over Japan (35°N, 136°E). *Tsuda et al.* [1990] find a strong summer and a weaker winter peak in GW wind fluctuations with still considerable amplitudes at equinoxes. The winter peak is associated with negative, i.e., westward momentum flux, the summer peak with positive, i.e., eastward momentum flux. The relative stronger summer maximum is compatible with the position of the MU radar close to the localized GW forcing due to the Asian monsoon.

6.2. Mean Flow Acceleration

[72] The GW-induced mean flow forcing is given by equation (42) of *Fritts and Alexander* [2003]:

$$(\bar{X}, \bar{Y}) = -\frac{\epsilon}{\bar{\rho}}\frac{\partial}{\partial z}(F_{px}, F_{py}), \tag{5}$$

where (F_{px}, F_{py}) is the horizontal vector of the vertical flux of GW pseudomomentum, $\bar{\rho}$ is the density of the background atmosphere, and $(\bar{X}, \bar{Y})$ an acceleration term for the

background flow. Conventionally, the equation contains an intermittency factor ϵ reflecting the fact that GWs might not always be present in the atmosphere. We calculate the acceleration for the GROGRAT composites as follows:

$$(\bar{X}, \bar{Y}) = -\frac{1}{\bar{\rho}} \frac{1}{J} \sum_i \epsilon_i \frac{\partial}{\partial z} \left(F_{px,i}, F_{py,i} \right), \qquad (6)$$

where J is the number of the individual GWs i in the considered bin (e.g., latitude bin at fixed altitude for zonal means) and ϵ_i is an intermittency factor associated with this wave according to Table 1. Note that in this way the final obliteration of a wave near a critical level does in our calculations not contribute to the acceleration, because we do not take into account the disappearance of waves between different altitude levels. However, the error due to this neglect is small, since the wave looses its momentum almost completely below: the vertical wavelength, and therefore the saturation amplitude, becomes very small before the GW encounters the critical level.

[73] In GROGRAT the waves can be horizontally refracted by horizontal gradients of the background atmosphere [*Marks and Eckermann*, 1995]. Therefore there are two different mechanisms for transferring momentum to the mean flow. First, the waves can dissipate by wave breaking or turbulent and radiative dissipation. In this case, the acceleration is given by the vertical gradient of the absolute value of momentum flux $|F_p|$ in the direction of the horizontal wave vector (k, l)

$$
\begin{aligned}
(\bar{X}, \bar{Y})_{diss} &= -\frac{1}{\bar{\rho}} \frac{1}{J} \sum_i \epsilon_i \frac{(k_i, l_i)}{k_i^2 + l_i^2} \frac{\partial}{\partial z} |F_{p,i}| \\
&= -\frac{1}{\bar{\rho}} \frac{1}{J} \sum_i \epsilon_i (\cos(\phi_i), \sin(\phi_i)) \frac{\partial}{\partial z} |F_{p,i}|, \qquad (7)
\end{aligned}
$$

where ϕ is the direction of the wave vector defined counterclockwise from due east ($\phi = 0$). Second, waves can change their horizontal propagation direction. For instance, a wave propagating northeastward might be aligned more zonally with increasing altitude due to lateral refraction. In this case, the wave carries less meridional and more zonal momentum. The acceleration is then expressed by the change of the wave direction and the acceleration by horizontal wave refraction is

$$(\bar{X}, \bar{Y})_{turn} = -\frac{1}{\bar{\rho}} \frac{1}{J} \sum_i \epsilon_i |F_{p,i}| \frac{\partial}{\partial z} (\cos(\phi_i), \sin(\phi_i)). \qquad (8)$$

[74] In addition to these two mechanisms there are further effects in GW theory which influence the momentum and amplitudes of GWs. When GWs are refracted by horizontal gradients of winds or buoyancy frequency also the absolute value of the horizontal wavelength and the area covered by the wave packet change. Without horizontal gradients rays launched at slightly different locations propagate on parallel raypaths. Including horizontal gradients of the background the rays converge or diverge (i.e., the area covered by one wave packet becomes smaller or larger) and simultaneously the horizontal wavelength becomes shorter or longer. Therefore these two effects would have to be considered simul-

taneously, but the geometric spreading effect cannot be incorporated easily into a model based on a very limited number of single rays. We therefore decided to neglect these effects and first investigate the GW forcing mechanisms described above.

[75] Figure 12 shows zonal mean accelerations for composite 5 for 15 July 2003. It should be noted that we do not apply SABER visibility filters for these acceleration fields. The left column shows the acceleration in the zonal direction and the right column the acceleration in the meridional direction. All waves which do not propagate purely zonally or purely meridionally contribute to both forcing terms. The uppermost row shows the total acceleration from equation (6). Values of $\bar{X}$ (Figure 12a) can reach up to $250 \text{ m s}^{-1} \text{ day}^{-1}$ at the summer mesopause (we clipped the color scale in order to better visualize the accelerations in the upper stratosphere and lower mesosphere). This is of the same order but at the high end of the acceleration values generally reported from GCM and GW parameterization studies [e.g., *McLandress*, 1998; *Charron et al.*, 2002; *McLandress and Scinocca*, 2005].

[76] The GROGRAT simulations include only medium-scale and large-scale GWs visible to SABER and do not include the short horizontal wavelength waves observed by airglow imagers [e.g., *Fritts and Alexander*, 2003; *Preusse et al.*, 2008]. Does the fact that the observed waves are already sufficient to explain all the wave forcing needed by the GCMs imply that medium and large horizontal wavelength GWs exclusively drive the MLT? This is a very interesting question, because from observations it cannot be satisfactorily estimated how the various horizontal wavelength ranges contribute in driving the large-scale flow [*Preusse et al.*, 2008]. In addition, recently GW resolving GCMs produced realistic mesospheric winds without using GW parameterizations [*Hamilton et al.*, 1999; *Watanabe*, 2008; *Becker*, 2009]. However, the evidence presented deduced from the SABER and CRISTA data is not sufficient to completely answer this question. When considering these values we should keep in mind that the GW accelerations shown are a pure forward result from the tuning of the launch values and intermittency factors by the measured GW amplitudes from SABER in July and some further constraints on GW momentum flux measurements in the stratosphere.

[77] As pointed out above, there is in particular a complete lack of constraints on the horizontal wavelength distribution in the mesosphere and thus there still remains great freedom for tuning. In addition, in our study some serious assumptions are made. For instance, we do not consider any processes that could transport momentum away from the dissipation regions such as secondary wave generation [*Vadas and Fritts*, 2002] or nonlinear wave interaction, for example, by triads [*Bittner et al.*, 1997; *Wüst and Bittner*, 2006]. We also assume that all waves propagate upward whereas in the real atmosphere at least some waves will propagate downward. The fraction of downward propagating waves is less than 20% according to data from radiosondes and radars for the lower stratosphere [e.g., *Wang et al.*, 2005; *Vaughan and Worthington*, 2007] and falling sphere data for the mid and upper stratosphere [e.g., *Eckermann and Vincent*, 1989]. It should be noted in this context that wave reflection occurs when the
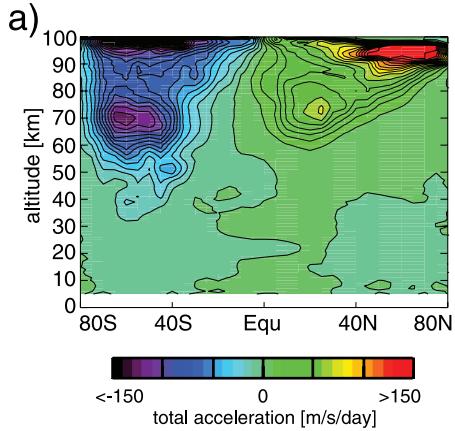
## Zonal Acceleration   Meridional Acceleration
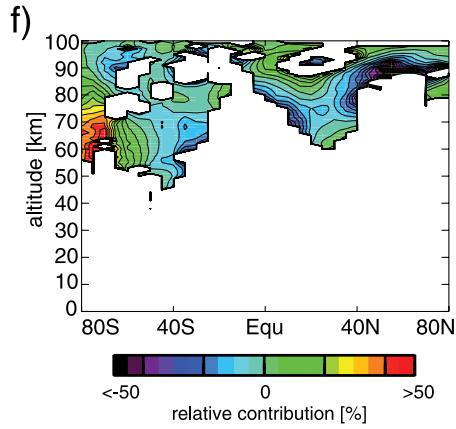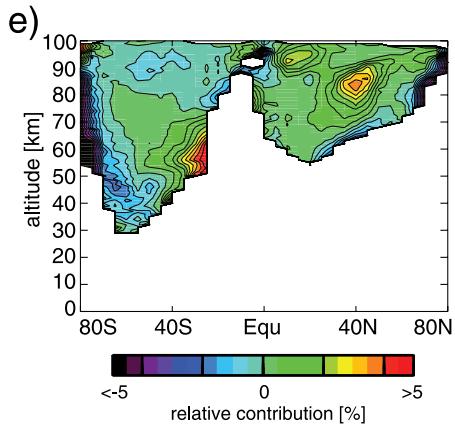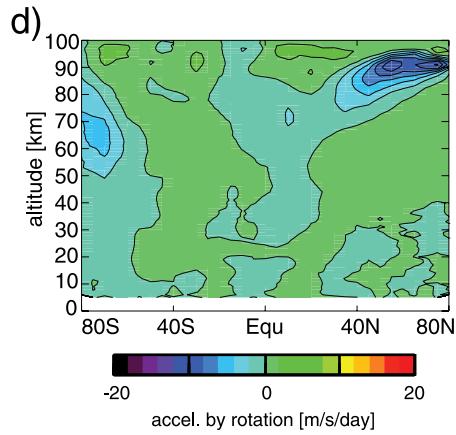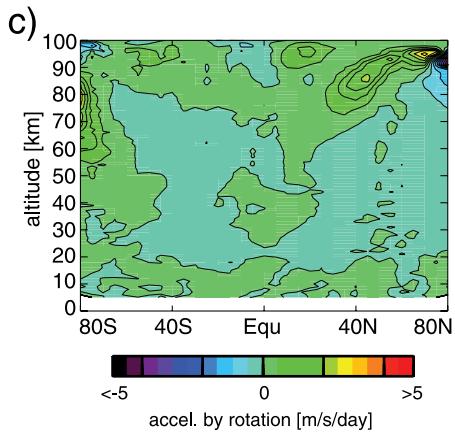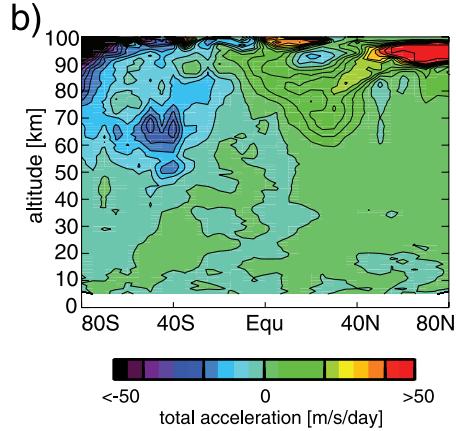
Figure 12. Zonal mean GW induced forcing for 15 July 2003 from GROGRAT for composite Experiment 5. (left) Zonal acceleration; (right) meridional acceleration. (a, b) The uppermost row gives the total values, (c, d) the middle row gives the acceleration due to horizontal refraction of the wave vector, and (e, f) the lowermost row shows the relative contribution that is attributed to horizontal refraction, i.e., Figures 12e and 12f give the percentage contribution of Figures 12c and 12d to the total forcing shown in Figures 12a and 12b.

intrinsic frequency $\hat{\omega}$ approaches the buoyancy frequency and does not occur to any great extent for the mesoscale and long horizontal wavelength (>100 km) GWs observed by IR limb sounders considered in this study [see *Kim et al.*, 2003; *Fritts and Alexander*, 2003; *Preusse et al.*, 2008]. Downward propagating waves in this wavelength regime therefore can only originate from high altitude sources.

[78] For the above mentioned reasons, our acceleration values are likely overestimated. Short horizontal wavelength GWs observed by airglow imagers are also known to carry significant momentum [*Tang et al.*, 2005]. Short and medium horizontal wavelength GWs therefore both contribute to driving the wind systems and circulation in the MLT. The uncertainties of this study are too large to
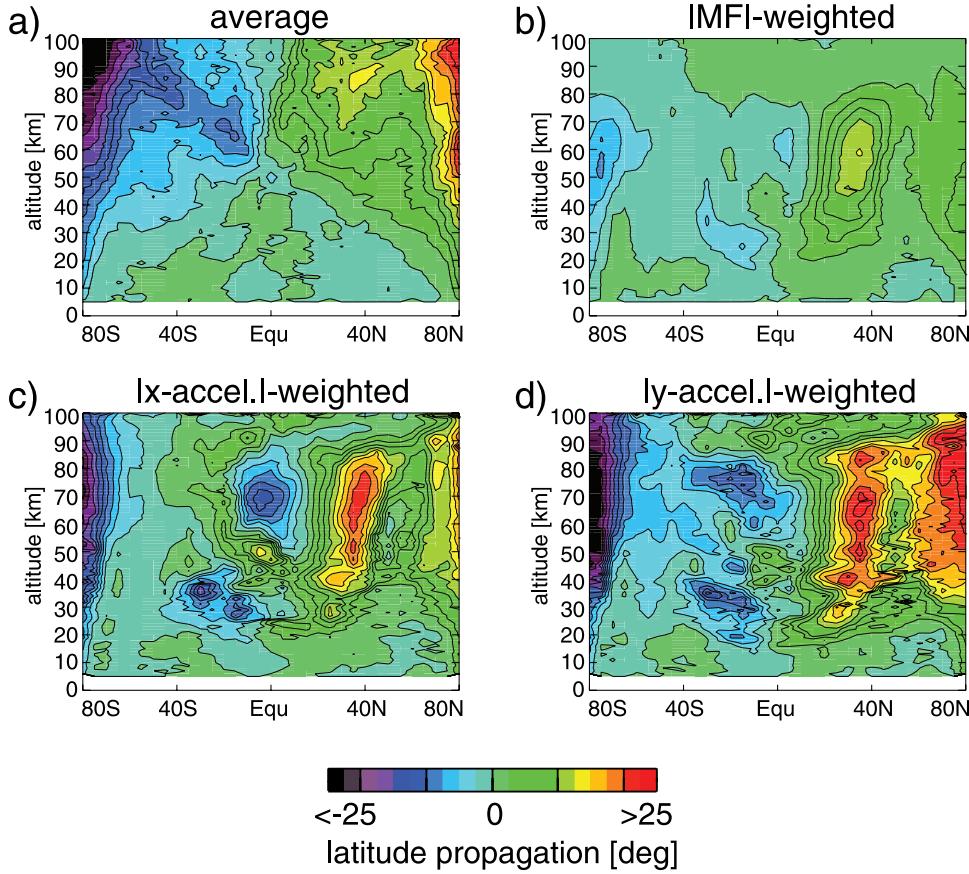
Figure 13. Zonal means of the latitude difference between the launch location and the point of observation. Model results for composite 5 are shown for 15 July 2003. (a) The average weighted only by the intermittency factors also used for the squared amplitudes and momentum flux values. (b) Additionally weighted by the absolute value of momentum flux of the individual waves. (c and d) Additionally weighted by the acceleration in the zonal and meridional direction.

definitively address the relative role of the different wavelength regimes quantitatively. However, the results shown suggest that medium-scale and large-scale gravity waves are important.

[79] Figure 12b shows the meridional acceleration $\overline{Y}$. The meridional accelerations are about a factor three smaller (again the color scale is clipped in order to highlight structures in the upper stratosphere and mesosphere). The fact that the meridional accelerations are smaller than the zonal accelerations is caused by the preferentially zonal direction of the mean flow.

[80] The middle row shows the contribution due to refraction by horizontal wind gradients calculated from equation (8). The lowermost row gives the relative contribution of this term to the total forcing. Relative values are only shown if the total acceleration is larger than 5 m s^{-1} day^{-1}. The zonal acceleration by horizontal refraction (Figure 12c) remains smaller than 5 m s^{-1} day^{-1} and contributes less than 5% of the total zonal mean flow acceleration (Figure 12e). Thus from the zonal GW induced forcing alone this effect could be neglected. Similar conclusions were drawn by *Hasha et al.* [2008]. However, the absolute values as well as the relative contributions in the meridional direction are larger (Figures 12d and 12f). Relative contributions of horizontal refraction to the merid-

ional forcing can exceed 50%. By comparing panels b and d it can be seen that horizontal refraction acts at different locations and sometimes counteracts acceleration by dissipation.

6.3. Cross-Latitudinal Propagation

[81] Gravity wave parameterization schemes operated in GCMs generally assume that GWs propagate upward in the vertical column of a GCM grid point. (There is one exception: the ray-tracing parameterization of convectively generated GWs by *Song and Chun* [2008].) However, since the GWs we consider have much longer horizontal than vertical wavelengths we can expect that they cover considerable distances in the horizontal when propagating from the troposphere into the mesosphere. An indication of this is given in Figure 1. Some of the waves shown traverse 40° or more in latitude. However, is this representative and are the waves that propagate over large distances the same waves which carry large momentum flux?

[82] Zonal means of the difference in latitude between the launch location and the actual position of the GW rays in the atmosphere are shown in Figure 13. Negative values indicate that the waves preferentially originate from sources northward of the observation latitude (i.e., southward-propagating waves), positive values indicate that the rays orig-

inate preferentially from the south (i.e., northward propagation). Low values can indicate a zonal alignment of the wave vectors and fast upward propagation or a balance between northward-propagating and southward-propagating waves.

[83] At very high latitudes we are close to the model grid boundaries and GWs propagating toward the lateral boundaries, i.e., poleward-propagating GWs, cannot be compensated by waves propagating in the opposite direction, since these waves would need to originate from outside the grid. The high values observed at very high latitudes (>60°) are therefore artificial and in the following we discuss low and mid latitudes (<60°) only.

[84] As expected, the average latitude shift increases with increasing altitude in Figure 13. A large part is contributed by long horizontal wavelength waves which can exist at low altitudes only in the tropics and spread poleward with increasing altitude (see Figure 2i). Consequently, when weighting the latitudinal shift by the momentum flux of the waves (Figure 13b), the values are strongly reduced. However, when weighting the latitudinal shift by the accelerations, in particular in the stratosphere and lower mesosphere the slower waves are emphasized and the latitudinal shift is enhanced. Even though accelerations at these altitudes are small they could contribute significantly to the branch of the Brewer-Dobson circulation in the summer hemisphere [*Alexander and Rosenlof*, 2003].

7. Summary and Discussion

[85] In this paper, we derived a climatology of GW squared amplitudes from the Sounding of the Atmosphere using Broadband Emission Radiometry (SABER) temperatures mapping a 5-year time series to calendar months. Many salient features are compatible with previous observations from different satellites showing these features to be persistent from year to year.

[86] The GW measurements are compared to results of global ray tracing simulations employing the Gravity wave Regional Or Global RAy Tracer (GROGRAT). Based on SABER zonal mean GW squared amplitudes for July and CRISTA momentum flux values, a homogeneous and isotropic launch distribution is iteratively tuned to best reproduce these observations. The resulting launch distribution contains different phase speed medium horizontal wavelength GWs, some of very high–phase speed and extremely low amplitudes, as well as long horizontal wavelength GWs of several thousand kilometer wavelength. Waves are launched in eight equispaced azimuth directions at 5 km altitude.

[87] The tuning of the launch distribution is based on zonal means of SABER GW squared amplitudes for July and CRISTA absolute values of momentum flux, only. Thereafter, no additional tuning is performed, and thus longitudinal structures seen in both measured and modeled global maps as well as time series of the annual cycle provide independent tests. The good agreement found in, e.g., reproducing observed seasonal variations raises confidence in the tuned GW launch parameters. In particular, the modeled time series reproduce an observed reversal of the phase of the annual cycle between 80 km and 95 km altitude. This phase reversal is attributed to medium-scale

horizontal wavelength GWs with ground-based horizontal-phase speeds greater than 50 m s^{-1}.

[88] Based on this cross-validated observation-tuned model run, we can calculate quantities which cannot be directly measured by SABER and are speculated to be major sources of uncertainty in current GW parameterization schemes. Two examples shown in this paper are the average cross-latitude propagation of GWs and the relative acceleration contributions provided by saturation and dissipation, on the one hand, and the horizontal refraction of GWs by horizontal gradients of the mean flow, on the other hand.

[89] The average cross-latitude propagation reaches peak values of about 15° in the upper mesosphere. Long horizontal wavelength waves carrying little momentum largely contribute to this value and as a consequence momentum flux–weighted mean values are much lower. However, acceleration-weighted values show up to 25° average cross-latitude propagation in the stratosphere and lower mesosphere. Though these accelerations are small in absolute value they can provide an important contribution to the summer-hemisphere branch of the Brewer-Dobson circulation [*Alexander and Rosenlof*, 2003]. In a changing climate, the wind fields in the troposphere and stratosphere will change. A propagation path of the waves that differs from the one assumed in tuning the parameterization scheme for the needs of the GCM then might induce an incorrect response to climate change.

[90] Both zonal and meridional GW induced mean flow acceleration values in the GROGRAT simulations are of the same order but at the upper end of the range known from GCM and GW parameterization scheme studies. Error ranges are high, however, since we have very few constraints on the horizontal wavelength distributions in particular of the fast waves carrying large momentum fluxes into the MLT. In addition, the current approach neglects processes which could carry away momentum flux from regions of wave instability, such as secondary wave generation.

[91] Despite these caveats we have a sufficiently realistic simulation to test whether the horizontal refraction of GWs by horizontal gradients of the background winds is an important effect on a global scale compared to momentum deposition by wave dissipation. Mean flow forcing by horizontal refraction was introduced by *Bühler and McIntyre* [2003] as a new mechanism acting at different locations and in a different way than wave dissipation via a process they referred to as "remote recoil". However, *Bühler and McIntyre* [2003] provided only a theoretical explanation of the effect and did not estimate the relative magnitude compared to wave dissipation in the real atmosphere. We here find that the effect is smaller than 5% for zonal acceleration in agreement to small influences reported by *Hasha et al.* [2008]. However, the effect is up to 50% in meridional acceleration and therefore merits further consideration.

[92] The GROGRAT model results match the observed distributions well. However, they give no hint on the physical nature of the assumed homogenous and isotropic sources. In addition, global maps already indicate missing localized sources such as orography and deep convection. In future, we therefore will need to replace a tuned parame-

terized source distribution by real understanding of lower atmospheric source distributions.

[93] In order to reach this aim a better characterization of the observed waves is required [*Alexander and Barnet*, 2007; *Eckermann et al.*, 2007]. Major sources of uncertainty for the current study are horizontal wavelength distributions and characteristics of propagation direction. Some first attempts to investigate horizontal wave structures were made by *Eckermann and Preusse* [1999] and *Preusse et al.* [2002], and recently some interesting studies have been based on nadir viewing instruments [*Wu and Zhang*, 2004; *Alexander and Barnet*, 2007; *Eckermann et al.*, 2006, 2007]. However, nadir viewing satellites can capture only a small part of the vertical wavelength distribution and only at the low altitudes (less than 40 km) where they are sensitive. What is urgently needed is an instrument with the good vertical resolution of a limb sounder and the good horizontal mapping of a nadir viewing instrument. Employing infrared limb imaging such an instrument can be built based on recent advances in detector technology [*Riese et al.*, 2005; *Friedl-Vallon et al.*, 2006].

Appendix A: Previous Work on Satellite Climatologies, Tuning to Observations, and GW Propagation

A1. Satellite Climatologies

[94] *Fetzer and Gille* [1994] were the first to demonstrate that satellite remote sensors can resolve GWs. During the last decade the number of instruments with sufficient spatial resolution to observe GWs has increased. Each type of instrument can detect only a certain part of the full vertical and horizontal wave number spectrum of GWs. Overviews and comparisons of different observation methods as well as the range of detectable vertical and horizontal wavelengths are given by *Wu et al.* [2006] and *Preusse et al.* [2008]. Infrared emission limb sounders have the advantage that they can resolve a wide range of vertical wavelengths.

[95] The SABER instrument has now operated for more than 6 years. This provides the opportunity to search for semiannual, annual and biennial variations of GW amplitudes [*Krebsbach and Preusse*, 2007; *Ern et al.*, 2008]. The long continuous measurements distinguish SABER from previous GW investigations of infrared limb emissions [e.g., *Fetzer and Gille*, 1994; *Eckermann and Preusse*, 1999; *Preusse and Ern*, 2005; *Ern et al.*, 2006], which cover a smaller altitude range and discuss (with the exception of the CLAES data [*Preusse and Ern*, 2005]) only selected time slices of one month or less.

A2. Measurement Model Intercomparison and Tuning to Observations

[96] Conventionally, global GW modeling starts with a semiempirical or process-based GW source distribution, propagates the waves through the background wind and temperature fields and compares the results to measured distributions. First attempts of this kind [*Eckermann*, 1992] used coarse spectral representations and limited data sets, more refined work [*Alexander*, 1998] was based on satellite [*Wu and Waters*, 1997] and *in situ* measurements [*Eckermann et al.*, 1995; *Allen and Vincent*, 1995] and on a finer spectral

representation. In addition, physics-based launch distributions were compared to satellite data [*Eckermann and Preusse*, 1999; *Jiang et al.*, 2002, 2004b]. Though in these cases the measurements were matched by the model hindcasts inside the range of uncertainty, *Jiang et al.* [2004b] concluded that there were still too many degrees of freedom to infer model improvements or identify model deficiencies. Only in the most recent studies [*Alexander and Rosenlof*, 2003; *Ern et al.*, 2006; *Preusse et al.*, 2006] quantitative constraints have been deduced from satellite measurements.

Appendix B: Physical Reasoning Behind the Different Distributions of Different SCEs

[97] In order not to distract from the main line of argument for selecting the intermittency factors we have summarized in section 4.2 only that different SCEs are fundamentally different, but not given the physical reasoning why this is the case. For those readers who are interested we here explain the different mechanisms leading to the different distributions.

[98] The effects of wind filtering and the correlation with background wind fields is strongest for the slow waves, for instance SCE 1 shown in Figure 2c. The strong latitudinal gradients observed in this panel are caused by three mechanisms, described in more detail by *Preusse et al.* [2006]. First, the waves are much slower than typical wind velocities in the stratosphere and the waves are therefore frequently subjected to critical level filtering when the ground-based horizontal-phase speed c_h matches the background wind velocity U in the direction of the wave vector ($c_h = U$). Second, the vertical wavelength is refracted by the background winds according to the approximate hydrostatic irrotational GW relation

$$\lambda_z = 2\pi \frac{|c_h - U|}{N},$$
(B1)

where λ_z is the vertical wavelength and N is the buoyancy frequency. (Equation (B1) is valid in the mid-frequency approximation $f^2 \ll \hat{\omega}^2 \ll N^2$.) Since N is about 0.02 s^{-1} in the stratosphere, a 5 km lower limit of the vertical wavelength visibility filter (i.e., the shortest vertical wavelength observable by SABER) corresponds to an intrinsic phase speed $|\hat{c}| = |c_h - U|$ of 16 m s^{-1}, which is much faster than the ground-based phase speed of these waves. These waves are thus only visible to SABER (and hence only appear in Figure 2), if they are refracted favorably by the background winds to large intrinsic phase speeds. This "visibility effect" was introduced by *Alexander* [1998]. Third, due to decreasing density waves grow in amplitude with increasing altitude. However, the maximum amplitude is limited by stability (saturation) criteria. If we assume convective instability to be the limiting process, the maximum temperature amplitude $\hat{T}_{\max}$ of a wave before breaking is related to the vertical wavelength by

$$\hat{T}_{\max} = \frac{N^2 \overline{T}}{2\pi g} \lambda_z,$$
(B2)

with $\overline{T}$ the background temperature and g Earth's gravitational acceleration. This equation is the mid-frequency approximation of the *Fritts and Rastogi* [1985] saturation

scheme we have used for our GROGRAT experiments. Waves propagating against the background wind attain larger vertical wavelengths and can have according to equation (B2) larger amplitudes.

[99] For the faster waves shown in the lower three rows of Figure 2, the lower limit of the visibility filter ($\lambda_z \geq 5$ km) is sufficiently short to retain most of the waves regardless of the background winds, and visibility effects are therefore less important for the distributions shown in panels d–i. For these SCEs, local maxima and horizontal structures are determined by the wave saturation amplitude and by whether the waves have achieved sufficient amplitudes to become saturated or not. The latter is the difference between panels d and e as well as f and g, respectively. The two SCEs shown in the left row are launched with higher launch amplitudes $\hat{u}_l$ than their counterparts in the right row. For instance, GW squared amplitudes for SCE 9 increase with altitude between 50 km and 60 km altitude. At these altitudes the values for SCE 7 remain almost constant, indicating saturation. Only above the saturation altitude do GW squared amplitudes form local maxima related to high wind velocities, and on top of the mesospheric jets the GW squared amplitudes decrease. In contrast, the waves shown in panel g (right column) never reach the saturation limit and steadily grow in amplitude with altitude.

[100] The steady increase of GW squared amplitudes observed in the SABER data (Figure 2b) at high altitudes is therefore an indication of the dominance of fast waves at high altitudes (>80 km). On the other hand, the low wave activity in the summer high latitudes at lower altitudes can only be matched by an SCE with a high saturation altitude and hence a low launch amplitude. The launch amplitudes given in Table 1 therefore demonstrate that if these waves originate in the troposphere or lower stratosphere (TLS) they could hardly be detected close to their source altitude by any measurement technique because of their very low amplitudes. On the other hand, this means that there is a good likelihood of such waves being forced by background fluctuations.

[101] Figure 2i shows long horizontal wavelength waves. Their ground-based frequency $\omega_{gb} = 2\pi c_h/\lambda_h$ is lower than the Coriolis parameter $|f|$ outside of the tropics. Compared to a phase speed of 30 m s^{-1} tropospheric wind speeds are, in genaral, too low to induce substantial Doppler shift and therefore at low altitudes these waves can only occur around the equator. At higher altitudes they can escape this confinement if they propagate opposite to strong background winds and therefore attain higher intrinsic frequencies. Long horizontal wavelength waves are therefore likely responsible for the tropical maximum observed in Figure 2b as well as in a number of previous in situ and satellite observations [*Alexander et al.*, 2002; *Ern et al.*, 2004; *Preusse et al.*, 2006].

[102] Fast waves of long horizontal wavelengths shown in Figure 2h are not strictly prohibited by the dispersion relation at higher latitudes, but are more likely subject to wave damping and critical level filtering than their shorter wavelength counterparts (e.g., the SCEs shown in panels f and g). Since they are also able to propagate far away from their sources, such waves can best match the slanted isolines of the SABER observations at mid and high northern latitudes (between 30°N and 70°N the isolines in Figure 2b have a slope close to 45°).

References

Alexander, M. J. (1998), Interpretations of observed climatological patterns in stratospheric gravity wave variance, *J. Geophys. Res.*, 103, 8627–8640.

Alexander, M. J., and C. Barnet (2007), Using satellite observations to constrain parameterizations of gravity wave effects for global models, *J. Atmos. Sci.*, 64, 1652–1665.

Alexander, M. J., and T. J. Dunkerton (1999), A spectral parameterization of mean-flow forcing due to breaking gravity waves, *J. Atmos. Sci.*, 56, 4167–4182.

Alexander, M. J., and K. H. Rosenlof (2003), Gravity-wave forcing in the stratosphere: Observational constraints from the Upper Atmosphere Research Satellite and implications for parameterization in global models, *J. Geophys. Res.*, 108(D19), 4597, doi:10.1029/2003JD003373.

Alexander, M. J., T. Tsuda, and R. A. Vincent (2002), On the latitudinal variations observed in gravity waves with short vertical wavelengths, *J. Atmos. Sci.*, 59, 1394–1404.

Allen, S. J., and R. A. Vincent (1995), Gravity wave activity in the lower atmosphere: Seasonal and latitudinal variations, *J. Geophys. Res.*, 100, 1327–1350.

Becker, E. (2009), Sensitivity of the upper mesosphere to the Lorenz energy cycle of the troposphere, *J. Atmos. Sci.*, 647–666, doi:10.1175/2008JAS2735.1.

Beldon, C. L., and N. J. Mitchell (2009), Gravity waves in the mesopause region observed by meteor radar: 2. Climatologies of gravity waves in the Antarctic and Arctic, *J. Atmos. Sol. Terr. Phys.*, in press.

Bittner, M., D. Offermann, and H. U. Widdel (1997), Nonlinear resonant interaction of atmospheric gravity waves derived from chaff-wind data: A case study, in *Proceedings 13th ESA Symposium on European Rocket and Balloon Programmes and Related Research*, Öland, Sweden, 26–29 May 1997, *ESA SP-397*, pp. 489–494.

Borsche, M., G. Kirchengast, and U. Foelsche (2007), Tropical tropopause climatology as observed with radio occultation measurements from CHAMP compared to ECMWF and NCEP analyses, *Geophys. Res. Lett.*, 34, L03702, doi:10.1029/2006GL027918.

Bühler, O., and M. E. McIntyre (2003), Remote recoil: A new wave-mean interaction effect, *J. Fluid Mech.*, 492, 207–230.

Burrage, M. D., R. A. Vincent, H. G. Mayr, W. R. Skinner, N. F. Arnold, and P. B. Hays (1996), Long-term variability in the equatorial middle atmosphere zonal wind, *J. Geophys. Res.*, 101, 12,847–12,854.

Charron, M., E. Manzini, and C. D. Warner (2002), Intercomparison of gravity wave parameterizations: Hines Doppler-spread and Warner and McIntyre ultra-simple schemes, *J. Meteorol. Soc. Jpn.*, 80, 335–345.

de la Torre, A., T. Schmidt, and J. Wickert (2006), A global analysis of wave potential energy in the lower and middle atmosphere from CHAMP and SAC-C GPS-RO long term data, *Geophys. Res. Lett.*, 33, L24809, doi:10.1029/2006GL027696.

Dörnbrack, A., and M. Leutbecher (2001), Relevance of mountain wave cooling for the formation of polar stratospheric clouds over Scandinavia: A 20 year climatology, *J. Geophys. Res.*, 106, 1583–1593.

Dowdy, A. J., R. A. Vincent, M. Tsutsumi, K. Igarashi, Y. Murayama, W. Singer, and D. J. Murphy (2007), Polar mesosphere and lower thermosphere dynamics: 1. Mean wind and gravity wave climatologies, *J. Geophys. Res.*, 112, D17104, doi:10.1029/2006JD008126.

Dunkerton, T. J. (1997), The role of gravity waves in the quasi-biennial oscillation, *J. Geophys. Res.*, 102, 26,053–26,076.

Eckermann, S. D. (1992), Ray-tracing simulation of the global propagation of inertia gravity waves through the zonally averaged middle atmosphere, *J. Geophys. Res.*, 97, 15,849–15,866.

Eckermann, S. D., and C. J. Marks (1997), GROGRAT: A new model of the global propagation and dissipation of atmospheric gravity waves, *Adv. Space Res.*, 20, 1253–1256.

Eckermann, S. D., and P. Preusse (1999), Global measurements of stratospheric mountain waves from space, *Science*, 286, 1534–1537.

Eckermann, S. D., and R. A. Vincent (1989), Falling sphere observations of anisotropic gravity wave motions in the upper stratosphere over Australia, *Pure Appl. Geophys.*, 130, 509–532.

Eckermann, S. D., I. Hirota, and K. W Hocking (1995), Gravity wave and equatorial wave morphology of the stratosphere derived from long-term rocket soundings, *Q. J. R. Meteorol. Soc.*, *121*, 146–186.

Eckermann, S. D., et al. (2006), Imaging gravity waves in lower stratospheric AMSU-A radiances: part 2. Validation case study, *Atmos. Chem. Phys.*, *6*, 3343–3362.

Eckermann, S. D., J. Ma, D. L. Wu, and D. Broutman (2007), A three-dimensional mountain wave imaged in satellite radiance throughout the stratosphere: Evidence of the effects of directional wind shear, *Q. J. R. Meteorol. Soc.*, *133*, 1959–1975.

Ern, M., P. Preusse, M. J. Alexander, and C. D. Warner (2004), Absolute values of gravity wave momentum flux derived from satellite data, *J. Geophys. Res.*, *109*, D20103, doi:10.1029/2004JD004752.

Ern, M., P. Preusse, and C. D. Warner (2006), Some experimental constraints for spectral parameters used in the Warner and McIntyre gravity wave parameterization scheme, *Atmos. Chem. Phys.*, *6*, 4361–4381.

Ern, M., P. Preusse, M. Krebsbach, M. G. Mlynczak, and J. M. Russell III (2008), Equatorial wave analysis from SABER and ECMWF temperatures, *Atmos. Chem. Phys.*, *8*, 845–869.

Fetzer, E. J., and J. C. Gille (1994), Gravity wave variances in LIMS temperatures: I. Variability and comparison with background winds, *J. Atmos. Sci.*, *51*, 2461–2483.

Friedl-Vallon, F., M. Riese, G. Maucher, A. Lengel, F. Hase, P. Preusse, and R. Spang (2006), Instrument concept and preliminary performance analysis of GLORIA, *Adv. Space Res.*, *37*, 2287–2291.

Fritts, D. C. (1984), Gravity wave saturation in the Middle Atmosphere: A review of theory and observations, *Rev. Geophys.*, *22*, 275–308.

Fritts, D. C., and P. K. Rastogi (1985), Convective and dynamical instabilities due to gravity wave motions in the lower and middle atmosphere: Theory and observations, *Radio Sci.*, *20*, 1247–1277.

Fritts, D. C., and M. J. Alexander (2003), Gravity wave dynamics and effects in the middle atmosphere, *Rev. Geophys.*, *41*(1), 1003, doi:10.1029/2001RG000106.

Gavrilov, N. M., S. Fukao, and T. Nakamura (2000), Gravity wave intensity and momentum fluxes in the mesosphere over Shigaraki, Japan (35N, 136E) during 1986–1997, *Ann. Geophys.*, *18*, 834–843.

Grossmann, K. U., D. Offermann, O. Gusev, J. Oberheide, M. Riese, and R. Spang (2002), The CRISTA-2 Mission, *J. Geophys. Res.*, *107*(D23), 8173, doi:10.1029/2001JD000667.

Hagan, M. E., J. M. Forbes, and F. Vial (1995), On modeling migrating solar tides, *Geophys. Res. Lett.*, *22*, 893–896.

Hamilton, K., R. J. Wilson, and R. S. Hemler (1999), Middle atmosphere simulated with high vertical and horizontal resolution versions of a GCM: Improvements in the cold pole bias and generation of a QBO-like oscillation in the tropics, *J. Atmos. Sci.*, *56*, 3829–3846.

Hasha, A., O. Bühler, and J. Scinocca (2008), Gravity wave refraction by three-dimensionally varying winds and the global transport of angular momentum, *J. Atmos. Sci.*, *65*, 2892–2906.

Hertzog, A., G. Boccara, R. A. Vincent, F. Vial, and Ph. Coquerez (2008), Estimation of gravity-wave momentum flux and phase speeds from long-duration stratospheric balloon flights: 2. Results from the Vorcore campaign in Antarctica, *J. Atmos. Sci.*, *65*, 3056–3070.

Hines, C. O. (1997), Doppler-spread parameterization of gravity-wave momentum deposition in the middle atmosphere: part 1. Basic formulation, *J. Atmos. Sol.-Terr. Phys.*, *59*, 371–386.

Hirota, I. (1978), Equatorial waves in upper stratosphere and mesosphere in relation to semiannual oscillation of zonal wind, *J. Atmos. Sci.*, *35*, 714–722.

Holton, J. R. (1982), The role of gravity wave induced drag and diffusion in the momentum budget of the mesosphere, *J. Atmos. Sci.*, *39*, 791–799.

Jiang, J. H., D. L. Wu, and S. D. Eckermann (2002), Upper Atmosphere Research Satellite (UARS) MLS observations of mountain waves over the Andes, *J. Geophys. Res.*, *107*(D20), 8273, doi:10.1029/2002JD002091.

Jiang, J. H., B. Wang, K. Goya, K. Hocke, S. D. Eckermann, J. Ma, D. L. Wu, and W. J. Read (2004a), Geographical distribution and interseasonal variability of tropical deep convection: UARS MLS observations and analyses, *J. Geophys. Res.*, *109*, D03111, 10.1029/2003JD003756.

Jiang, J. H., S. D. Eckermann, D. L. Wu, and J. Ma (2004b), A search for mountain waves in MLS stratospheric limb radiances from the winter Northern Hemisphere: Data analysis and global mountain wave modeling, *J. Geophys. Res.*, *109*, D03107, doi:10.1029/2003JD003974.

Kim, Y. J., S. D. Eckermann, and H.-Y. Chun (2003), An overview of the past, present and future of gravity-wave drag parametrization for numerical climate and weather prediction models - survey article, *Atmos.-Ocean*, *41*, 65–98.

Krebsbach, M., and P. Preusse (2007), Comparison of global distributions of zonal-mean gravity wave variance inferred from different satellite measurements, *Geophys. Res. Lett.*, *34*, L03814, doi:10.1029/2006GL028040.

Kutepov, A. A., A. G. Feofilov, B. T. Marshall, L. L. Gordley, W. D. Pesnell, R. A. Goldberg, and J. M. Russell III (2006), SABER temperature observations in the summer polar mesosphere and lower thermosphere: Importance of accounting for the CO2 ν2 quanta V-V exchange, *Geophys. Res. Lett.*, *33*, L21809, doi:10.1029/2006GL026591.

Manzini, E., and N. A. McFarlane (1998), The effect of varying the source spectrum of a gravity wave parameterization in a middle atmosphere general circulation model, *J. Geophys. Res.*, *103*, 31,523–31,539.

Marks, C. J., and S. D. Eckermann (1995), A three-dimensional nonhydrostatic ray-tracing model for gravity waves: Formulation and preliminary results for the middle atmosphere, *J. Atmos. Sci.*, *52*, 1959–1984.

McLandress, C. (1998), On the importance of gravity waves in the middle atmosphere and their parameterization in general circulation models, *J. Atmos. Sol.-Terr. Phys.*, *60*, 1357–1383.

McLandress, C., and J. F. Scinocca (2005), The GCM response to current parameterizations of nonorographic gravity wave drag, *J. Atmos. Sci.*, *62*, 2394–2413.

McLandress, C., M. J. Alexander, and D. L. Wu (2000), Microwave limb sounder observations of gravity waves in the stratosphere: A climatology and interpretation, *J. Geophys. Res.*, *105*, 11,947–11,967.

Medvedev, A. S., and G. P. Klaassen (2000), Parameterization of gravity wave momentum deposition based on nonlinear wave interactions: Basic formulation and sensitivity tests, *J. Atmos. Sol.-Terr. Phys.*, *62*, 1015–1033.

Mertens, C. J., M. G. Mlynczak, M. Lopez-Puertas, P. P. Wintersteiner, R. H. Picard, J. R. Winick, L. L. Gordley, and J. M. Russell III (2001), Retrieval of mesospheric and lower thermospheric kinetic temperature from measurements of CO_2 15 μm Earth limb emission under non-LTE conditions, *Geophys. Res. Lett.*, *28*, 1391–1394.

Mertens, C. J., et al. (2004), SABER observations of mesospheric temperatures and comparisons with falling sphere measurements taken during the 2002 summer MaCWAVE campaign, *Geophys. Res. Lett.*, *31*, L03105, doi:10.1029/2003GL018605.

Mlynczak, M. G. (1997), Energetics of the mesosphere and lower thermosphere and the SABER experiment, *Adv. Space Res.*, *20*(6), 1177–1183.

Oberheide, J., Q. Wu, T. L. Killeen, M. E. Hagan, and R. G. Roble (2006), Diurnal nonmigrating tides from TIDI wind data: Monthly climatologies and seasonal variations, *J. Geophys. Res.*, *111*, A10S03, doi:10.1029/2005JA011491.

Offermann, D., K. U. Grossmann, P. Barthol, P. Knieling, M. Riese, and R. Trant (1999), The cryogenic infrared spectrometers and telescopes for the atmosphere (CRISTA) experiment and middle atmosphere variability, *J. Geophys. Res.*, *104*, 16,311–16,325.

Preusse, P., and M. Ern (2005), Indication of convectively generated gravity waves observed by CLAES, *Adv. Space Res.*, *35*, 1987–1991, doi:10.1016/j.asr.2004.09.005.

Preusse, P., S. D. Eckermann, J. Oberheide, M. E. Hagan, and D. Offermann (2001a), Modulation of gravity waves by tides as seen in CRISTA temperatures, *Adv. Space Res.*, *27*, 1773–1778.

Preusse, P., G. Eidmann, S. D. Eckermann, B. Schaeler, R. Spang, and D. Offermann (2001b), Indications of convectively generated gravity waves in CRISTA temperatures, *Adv. Space Res.*, *27*, 1653–1658.

Preusse, P., A. Dörnbrack, S. D. Eckermann, M. Riese, B. Schaeler, J. Bacmeister, D. Broutman, and K. U. Grossmann (2002), Space based measurements of stratospheric mountain waves by CRISTA: 1. Sensitivity, analysis method and a case study, *J. Geophys. Res.*, *107*(D23), 8178, doi:10.1029/2001JD000699.

Preusse, P., et al. (2006), Tropopause to mesopause gravity waves in August: Measurement and modeling, *J. Atmos. Sol.-Terr. Phys.*, *68*, 1730–1751.

Preusse, P., S. D. Eckermann, and M. Ern (2008), Transparency of the atmosphere to short horizontal wavelength gravity waves, *J. Geophys. Res.*, *113*, D24104, doi:10.1029/2007JD009682.

Remsberg, E. E., et al. (2008), Assessment of the quality of the Version 1.07 temperature-versus-pressure profiles of the middle atmosphere from TIMED/SABER, *J. Geophys. Res.*, *113*, D17101, doi:10.1029/2008JD010013.

Riese, M., R. Spang, P. Preusse, M. Ern, M. Jarisch, D. Offermann, and K. U. Grossmann (1999), Cryogenic infrared spectrometers and telescopes for the atmosphere (CRISTA) data processing and atmospheric temperature and trace gas retrieval, *J. Geophys. Res.*, *104*, 16,349–16,367.

Riese, M., F. Friedl-Vallon, R. Spang, P. Preusse, C. Schiller, L. Hoffmann, P. Konopka, H. Oelhaf, T. von Clarmann, and M. Höpfner (2005), Global limb radiance imager for the atmosphere (GLORIA): Scientific objectives, *Adv. Space Res.*, *36*, 989–995.

Roble, R. G., and E. C. Ridley (1994), A thermosphere-ionosphere-mesosphere-electrodynamics general circulation model (TIME-GCM): Equinox solar cycle minimum simulations (30–500 km), *Geophys. Res. Lett.*, *21*, 417–420.

Russell, J. M., III, M. G. Mlynczak, L. L. Gordley, J. Tansock, and R. Esplin (1999), An overview of the SABER experiment and preliminary calibration results, *Proc. SPIE*, *3756*, 277–288.

Song, I.-S., and H.-Y. Chun (2008), A Lagrangian spectral parameterization of gravity wave drag induced by cumulus convection, *J. Atmos. Sci.*, *65*, 1204–1224.

Tang, J., G. R. Swenson, A. Z. Liu, and F. Kamalabadi (2005), Observational investigations of gravity wave momentum flux with spectroscopic imaging, *J. Geophys. Res.*, *110*, D09S09, doi:10.1029/2004JD004778.

Thorsen, D., and S. J. Franke (1998), Climatology of mesospheric gravity wave activity over Urbana, Illinois (40N, 88W), *J. Geophys. Res.*, *103*, 3767–3780.

Tsuda, T., and K. Hocke (2002), Vertical wave number spectrum of temperature fluctuations in the stratosphere using GPS occultation data, *J. Meteorol. Soc. Jpn.*, *80*, 925–938.

Tsuda, T., Y. Murayama, M. Yamamoto, S. Kato, and S. Fukao (1990), Seasonal variation of momentum flux in the mesosphere observed with the MU radar, *Geophys. Res. Lett.*, *17*, 725–728.

Tsuda, T., M. Nishida, C. Rocken, and R. H. Ware (2000), A global morphology of gravity wave activity in the stratosphere revealed by the GPS Occultation data (GPS/MET), *J. Geophys. Res.*, *105*, 7257–7273.

Vadas, S. L., and D. C. Fritts (2002), The importance of spatial variability in the generation of secondary gravity waves from local body forces, *Geophys. Res. Lett.*, *29*(20), 1984, doi:10.1029/2002GL015574.

Vaughan, G., and R. M. Worthington (2007), Inertia-gravity waves observed by the UK MST radar, *Q. J. R. Meteorol. Soc.*, *133*, 179–188.

Vincent, R. A., and D. C. Fritts (1987), A climatology of gravity wave motions in the mesopause region at Adelaide, Australia, *J. Atmos. Sci.*, *44*, 748–760.

Wang, L., M. A. Geller, and M. J. Alexander (2005), Spatial and temporal variations of gravity wave parameters: part I. Intrinsic frequency, wavelength, and vertical propagation direction, *J. Atmos. Sci.*, *62*, 125–142.

Warner, C. D., and M. E. McIntyre (1999), Toward an ultra-simple spectral gravity wave parameterization for general circulation models, *Earth Planets Space*, *51*, 475–484.

Watanabe, S. (2008), Constraints on a non-orographic gravity wave drag parameterization using a gravity wave resolving general circulation model, *Sci. Online Lett. Atmos.*, *4*, 61–64.

Wu, D. L., and J. W. Waters (1997), Observations of gravity waves with the UARS Microwave Limb Sounder, in *Gravity Wave Processes and Their Parametrization in Global Climate Models*, edited by K. Hamilton, Springer, New York.

Wu, D. L., and F. Zhang (2004), A study of mesoscale gravity waves over the North Atlantic with satellite observations and a mesoscale model, *J. Geophys. Res.*, *109*, D22104, doi:10.1029/2004JD005090.

Wu, D. L., and S. D. Eckermann (2008), Global gravity wave variances from Aura MLS: Characteristics and interpretation, *J. Atmos. Sci.*, *65*, 3695–3718.

Wu, D. L., P. Preusse, S. D. Eckermann, J. H. Jiang, M. de la Torre Juarez, L. Coy, B. Lawrence, and D. Y. Wang (2006), Remote sounding of atmospheric gravity waves with satellite limb and nadir techniques, *Adv. Space Res.*, *37*, 2269–2277.

Wüst, S., and M. Bittner (2006), Non-linear resonant wave-wave interaction (triad): Case studies based on rocket data and first application to satellite data, *J. Atmos. Sol.-Terr. Phys.*, *68*, 959–976.

Yee, J. H., E. R. Talaat, A. B. Christensen, T. L. Killeen, J. M. Russell, and T. N. Woods (2003), TIMED instruments, *Johns Hopkins APL Tech. Dig.*, *24*(2), 156–164.

————————————

S. D. Eckermann, Space Science Division, Code 7646, Naval Research Laboratory, Washington, DC 20375-5352, USA. (stephen.eckermann@nrl.navy.mil)

M. Ern, P. Preusse, and M. Riese, Forschungszentrum Juelich GmbH, Institute of Chemistry and Dynamics of the Geosphere, ICG-1: Stratosphere, Research Center Juelich, 52425 Juelich, Germany. (p.preusse@fz-juelich.de)

M. G. Mlynczak, NASA Langley Research Center, Hampton, VA 23681-0001, USA.

J. Oberheide, Department of Physics, Wuppertal University (BUGW), Gauss Str. 20, D-42097 Wuppertal, Germany.

R. H. Picard, Air Force Research Laboratory (RVBYM), 29 Randolph Road, Hanscom AFB, MA 01731-3010, USA.

R. G. Roble, High Altitude Observatory, National Center for Atmospheric Research, 3450 Mitchell Lane, Boulder, CO 80307, USA.

J. M. Russell III, Center for Atmospheric Sciences, Hampton University, Hampton, VA 23668, USA.